

Toward Platinum Group Metal-Free Catalysts for Hydrogen/Air Proton-Exchange Membrane Fuel Cells

Catalyst activity in platinum-free substitute cathode and anode materials

Frédéric Jaouen*, Deborah Jones

Institut Charles Gerhardt Montpellier, CNRS - Université Montpellier - ENSCM, Place Eugene Bataillon, 34095 Montpellier cedex 5, France

Nathan Coutard, Vincent Artero#

Laboratoire de Chimie et Biologie des Métaux, Université Grenoble Alpes, CNRS, CEA, 17 rue des Martyrs, 38054 Grenoble cedex 9, France

Peter Strasser

Technische Universität Berlin, Institut für Chemie, Strasse des 17. Juni 124, 10623 Berlin, Germany

Anthony Kucernak

Department of Chemistry, Imperial College London, South Kensington Campus, London, SW7 2AZ, UK

Email: *frederic.jaouen@umontpellier.fr, #vincent.artero@cea.fr

The status, opportunities and challenges toward catalysts free of platinum group metal (pgm) elements for proton-exchange membrane fuel cells (PEMFC) are reviewed. Due to the limited reserves of noble metals in the Earth's crust, a major challenge for the worldwide development of PEMFC technology is to replace Pt with pgm-free catalysts with sufficient activity and stability. The priority target is the substitution of cathode catalysts (oxygen reduction) that account for more than 80% of pgms in current PEMFCs. Regarding hydrogen oxidation at the anode,

ultralow Pt content electrodes have demonstrated good performance, but alternative non-pgm anode catalysts are desirable to increase fuel cell robustness, decrease the H₂ purity requirements and ease the transition from H₂ derived from natural gas to H₂ produced from water and renewable energy sources.

1. Introduction

1.1 Opportunities for PEMFCs

Electromobility developments, and PEMFCs in particular, are under intense development for a cleaner and more efficient use of energy, including the use of renewable electricity for transportation (1). While rechargeable batteries directly store and discharge electric power, H₂/air PEMFCs convert the chemical energy of H₂ into electricity and heat. Today, the lion's share of H₂ production comes from natural gas. In the future, H₂ could however be produced at competitive price and with lower environmental impact from water and renewable energy. The power-to-gas and gas-to-power consecutive conversions needed to use H₂ as an energy carrier might seem *a priori* less attractive than the reversible storage of electricity in batteries due to its higher complexity and lower roundtrip energy efficiency. However, technical requirements and customer acceptance favour fuel cells over batteries for certain markets. In the automotive sector for example, lithium-ion battery electric vehicles (BEV) offer shorter driving range than internal combustion engine (ICE) vehicles. In contrast, H₂-powered PEMFC vehicles have already demonstrated a

driving range of 500 km and refuelling time of less than 4 min (2, 3). Whether battery or fuel cell, the electrification of the automobile could significantly cut carbon dioxide emissions (25% of CO₂ emissions originated from the transport set or in 2010 (4)) and reduce our reliance on fossil fuels. Otherwise, CO₂ emissions from road transportation will continue increasing over the next decades, due to an increased global fleet of vehicles (Figure 1).

H₂ is often perceived as more dangerous than gasoline-fuelled ICE. However the low density of H₂ naturally prevents the detonation limit from

being reached in an unconfined space. BEVs are distinctly associated with low driving range and the difficulty in knowing the instantaneous state-of-charge of a battery (5). Considering systems able to deliver the same electric power (kW), the weight of a H₂-tank/PEMFC stack system becomes systematically lower than that of a rechargeable Li-battery above a certain threshold amount of energy (kWh). While the exact threshold value depends on the technology status and also on the mass of the air, threshold values of 20–30 kWh have been estimated (1, 2). As a comparison, 10 kWh is the

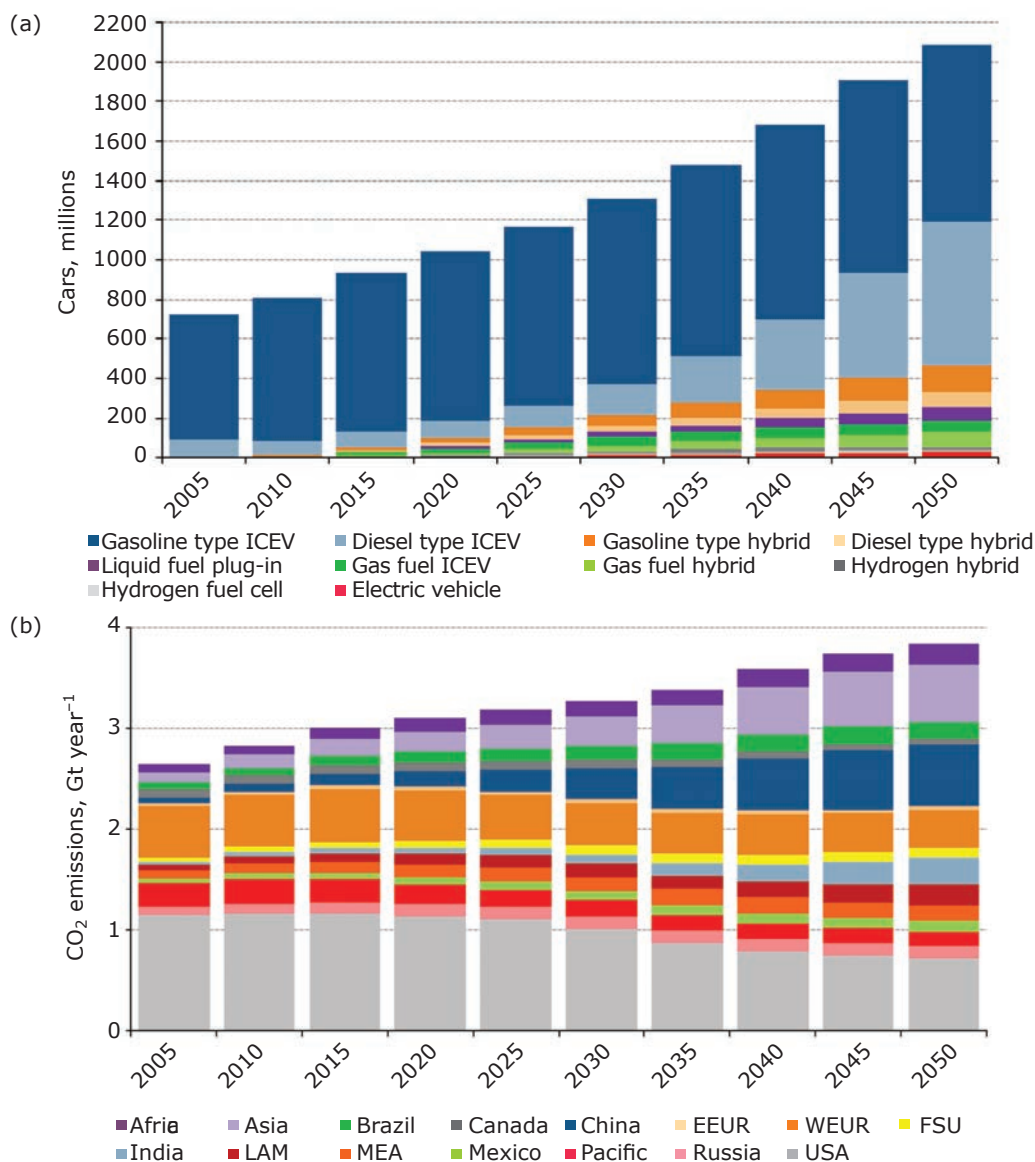


Fig. 1. (a) Assumed technology mix for cars until 2050 (million vehicles); (b) predicted CO₂ emissions from cars (gigatonnes CO₂ year⁻¹). Reproduced from (4). The model assumes that global car fleet remains dominated by gasoline and diesel ICE (78%), a significant share of hybrid vehicles (18%) and a small fraction of EVs (4%). Key: ICEV = internal combustion engine vehicle; EEUR = Eastern Europe; WEUR = Western Europe; FSU = Former Soviet Union; LAM = Latin America; MEA = Middle East and Africa. Used by permission of the World Energy Council, London, www.worldenergy.org

electrical energy needed to move a mid-size car over 100 km (1).

While a BEV with longer driving range needs a proportionally higher mass of battery to store more energy, a H₂-tank/PEMFC system only needs a larger tank to store more energy, with low associated incremental mass. This simple fact favours H₂-PEMFC systems for transport applications requiring long driving range (Figure 2). However, when a short driving range is acceptable, BEVs are

more energy efficient than fuel cells (2). Pure BEVs and fuel cell electric vehicles (FCEV) may therefore target different segments of the automotive market (1). Other important applications of PEMFCs are as backup power systems, and for combined heat and power (CHP) (6). For backup power, the chemical energy contained in H₂ can be stored for years without 'discharge'. For CHP, the cell voltage of the PEMFC can be advantageously controlled during operation to tune the electrical and thermal power

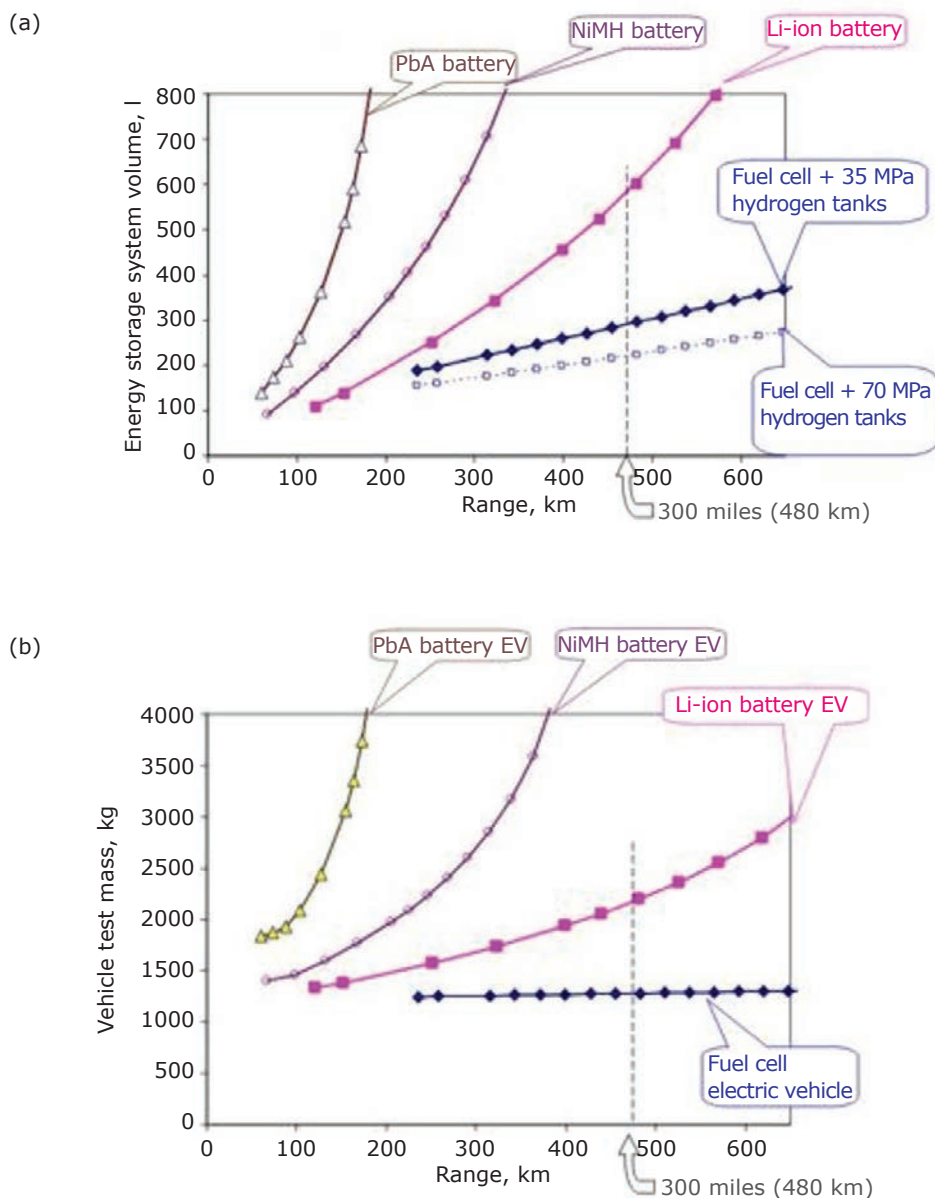


Fig. 2. (a) Calculated energy storage system volume for an electric vehicle (EV) equipped either with a compressed-H₂ storage/PEMFC system or with various battery technologies as a function of the vehicle range; (b) same comparison but for the estimated mass of the energy storage and conversion system. The power trains are adjusted to provide a zero to 97 km h⁻¹ acceleration time of 10 s. Reproduced from (2) with permission from Elsevier

outputs. About 140,000 PEMFC units for CHP have been installed in Japan between 2009 and 2015 and this application is also taking off in South Korea and Europe (6).

The remaining technical challenges for PEMFCs are lowered cost and improved durability, with the electrode catalysts and membrane ionomer materials being at the heart of the vital functions and lifetime of a PEMFC. While at low production volumes, the global demand of Pt for PEMFCs is not high and the share of the Pt cost in the PEMFC stack cost is not excessive, both those variables would increase dramatically in the case of a massive deployment of PEMFCs. The share of Pt catalyst to fuel cell stack cost would increase due to decreased cost for all other components through economies of scale (Figure 3) (7). Assuming a constant Pt price over time and unchanged Pt mass per rated power of PEMFC ($\text{kW}_{\text{electric}}$), the stack cost would reach a lower-value plateau, nearly incompressible upon further increased production volumes. In parallel, the ratio of Pt-to-stack cost would increase to ca. 50% (Figure 3). It must be noted that this percentage is a conservative estimation, reached assuming a constant Pt price. It is likely, however, that the scarcity of Pt combined with increased demand would lead to increased price. This could possibly lead to an increased stack cost (instead of a levelled-off cost above ca. 100,000 units per year),

above a certain threshold of volume production. This may impede reaching (or staying at, in the case of millions of units produced per year) the cost target of $\text{US}\$20 \text{ kW}_{\text{electric}}^{-1}$ for an automotive PEMFC stack (8). Reaching but also staying at this cost is necessary for PEMFCs to be cost competitive with ICE and affordable to the wide public.

The particular importance of the cathode catalyst (oxygen reduction reaction (ORR) catalysis) is introduced in Section 2, while the anode catalyst (hydrogen oxidation reaction (HOR) catalysis) opportunities are discussed in Section 3. This review gives a focused account of recent achievements and discusses the needs and possibilities toward the rational design of improved non-pgm cathode catalysts. Comprehensive reviews and book chapters on pyrolysed metal-nitrogen-carbon (Me-N-C, where 'Me' is a transition metal) cathode catalysts and inorganic non-pgm anode catalysts for PEMFCs can be found elsewhere (9–12).

2. Non-pgm Cathode Catalysts

2.1 The Need for Non-pgm Cathode Catalysts

Due to the much slower kinetics of the ORR than those of the HOR on Pt surfaces, 80–90% of Pt in

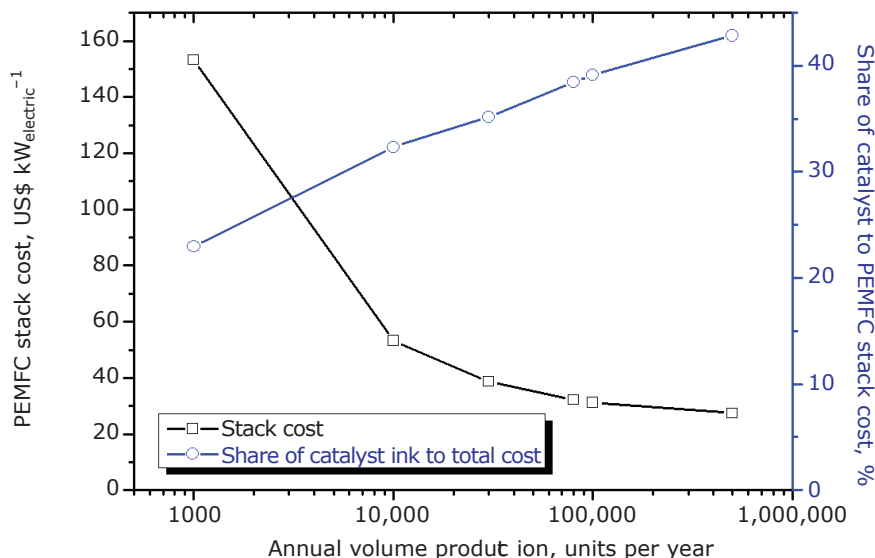


Fig. 3. Predicted automotive PEMFC stack cost as a function of annual volume production. The predicted cost is based on the 2016 automotive technology, including in particular $0.21 \text{ g}_{\text{Pt}} \text{ kW}_{\text{el}}$ ($0.116 \text{ mg}_{\text{Pt}} \text{ cm}^{-2}$ at cathode, $0.018 \text{ mg}_{\text{Pt}} \text{ cm}^{-2}$ at anode). Graph drawn from data in (7), data used with permission from Strategic Analysis Inc, USA

H₂-fuelled PEMFCs is currently positioned at the cathode (13). In this context, the development of Pt-based catalysts with higher ORR activity normalised per mass Pt is under intense investigation (14–16), with the practical objective of reducing the Pt content in automotive PEMFC stacks down to the current pgm content in catalytic converters of ICE-powered automobiles (1–4 g depending on vehicle size, engine types and local regulations on air quality). The very high ORR activity of some Pt nanostructures (such as Pt nanoframes or jagged nanowires) recently observed in rotating-disk-electrode measurements remain to be transposed to the PEMFC environment, and their long-term durability proven. In addition, a very high turnover frequency for the ORR on a small number of active sites in the cathode, while being a dream for electrocatalysis scientists, may turn out to be an issue for membrane electrode assembly (MEA) developers due to enhanced local O₂ diffusion barriers in a PEMFC cathode with low volumetric density of active sites (17, 18). The replacement of Pt-based catalysts with pgm-free cathode catalysts is considered a holy grail. Ideally, highly active and durable pgm-free cathode catalysts could replace Pt-based cathodes in PEMFCs designed for all types of markets. Alternatively, pgm-free cathodes not meeting the stringent durability and power performance targets of the automotive industry may be competitive for other applications (for example, backup power, mobile applications or CHP) (16).

The pgm-free materials that have hitherto displayed the highest ORR activity when tested in aqueous acid medium or in single-cell PEMFC are pyrolysed Me-N-C catalysts, with the metal being iron or cobalt (19, 20). Me-N-C catalysts have been prepared from numerous precursors of metal, nitrogen and carbon *via* the optimisation of the precursor ratio, metal content and pyrolysis conditions that must be adapted to each system of precursors (10). The nature of the metal-based active sites in sub-Me-N-C catalysts is fundamentally different from that in Pt-based catalysts (compare **Figures 4(b), 4(c)** and **4(d)** to **Figure 4(a)**). The most active sites for ORR in pyrolysed Me-N-C catalysts are, from the most recently established knowledge, single metal-ions strongly coordinated with nitrogen ligands (MeN_x moieties, *x* being on average 4), and these MeN_x moieties are covalently integrated in graphene, or disordered graphene, sheets (**Figure 4**) (21, 22, 23–25). The local coordination of sub-MeN_x moieties resembles the metal-ion coordination in phthalocyanine and porphyrin compounds (23), but their covalent integration in the electrode

matrix distinguishes them from these well-defined organic compounds, and is critical to reach high current densities in PEMFC.

2.2 Concepts for the Design of Me-N-C Catalysts and Catalyst Layers

Research and development (R&D) efforts and interest in non-pgm catalysts for the ORR in acid medium have never been so intense, as witnessed by a rising number of research groups working on the topic but also an increasing number of R&D funding efforts dedicated to this class of catalysts, for example in Europe from the Fuel Cells and Hydrogen 2 Joint Undertaking (FCH 2 JU) (26), and in the USA from the US Department of Energy (DOE) (27). In the USA, R&D efforts in non-pgm catalysts for PEMFC are now organised by the ElectroCatalysis Consortium (ElectroCat). A broader initiative to reduce the reliance on Critical Raw Materials and increase their recycling was also initiated by the European Union (EU) for various new energy technologies (28). Two companies are currently engaged in the development of Me-N-C and other non-pgm catalysts for PEMFCs (Pajarito Powder, USA and Nisshinbo Holdings, Japan). In September 2017, Ballard, Canada, and Nisshinbo Holdings announced the first portable PEMFC (30 W) commercialised with a non-pgm cathode catalyst (29). This interest in Me-N-C catalysts and user shift towards application is the result of important progress in the field since 2009, with breakthroughs achieved in the ORR activity reached at high cell voltage in single-cell PEMFC (30), power density at cell voltage experienced during practical operation (0.5–0.7 V range) (22, 31), and understanding of the nature of the active sites (21, 22, 23, 25) and how they catalyse the ORR at atomistic level (24, 32, 33). **Table I** gives examples of synthesis strategies and corresponding ORR current density measured in PEMFC at 0.9 V (ORR 'activity') for some of the most active Fe-N-C catalysts to date. The cathode catalyst loading used in each work is also indicated in the second column (mg_{Fe-N-C} cm⁻²). Within a certain range (typically 0.5 mg_{Fe-N-C} cm⁻² to 5 mg_{Fe-N-C} cm⁻²), the current density at 0.9 V increases proportionally with cathode catalyst loading. Based on this, the current density at 0.9 V expected for a loading of 5 mg_{Fe-N-C} cm⁻² is indicated in the third column in **Table I**. It must be noted that proportionally increased current density with increased cathode loading is restricted to low current. At high current density (>200 mA cm⁻²), the cell performance is also impacted by mass- and

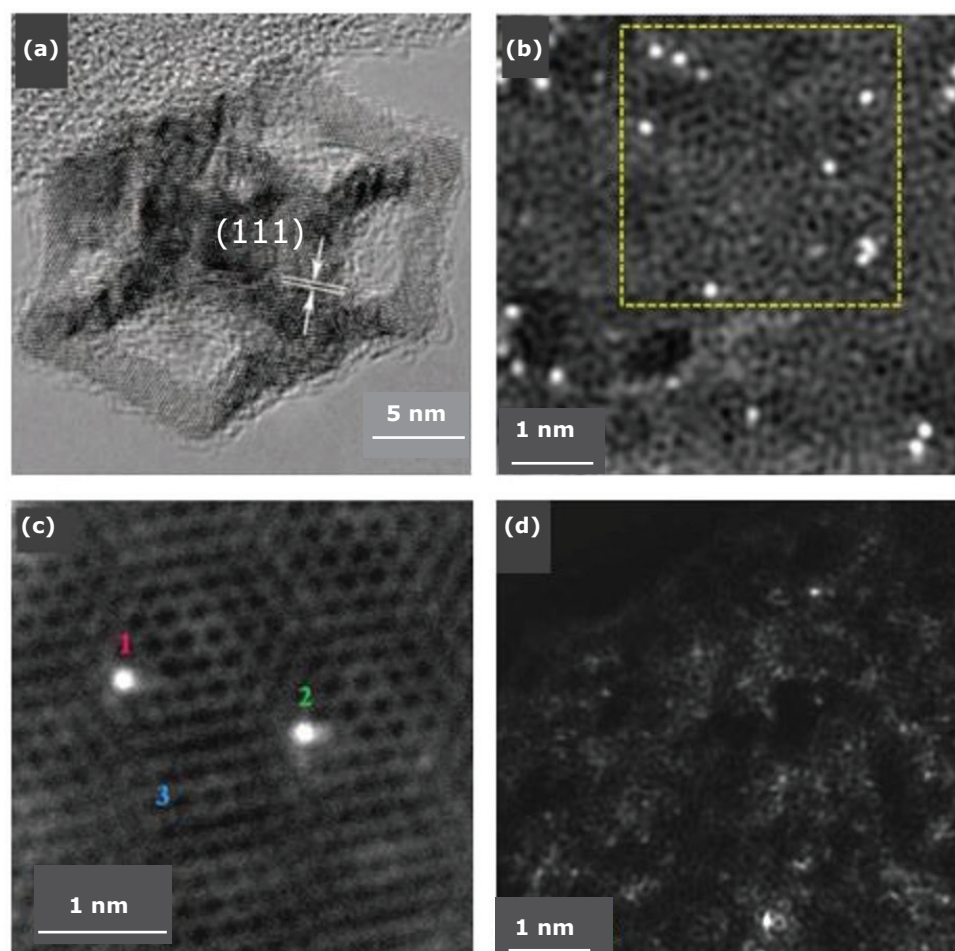


Fig. 4. The crystallographic ordering of Pt atoms in Pt-based catalysts and the atomically-dispersed nature of Fe and Co atoms in pyrolysed Fe(Co)-N-C catalysts, as revealed by high-resolution scanning transmission electron microscopy (HR-STEM) images: (a) Pt₃Ni nanoframe, from (14). Reprinted with permission from AAAS; (b) Co-N-C catalyst obtained *via* pyrolysis in ammonia of a cobalt salt and graphene, showing atomically dispersed cobalt in the N-doped carbon matrix, reproduced from (21); (c) Fe-N-C catalyst prepared from a ferrous salt, aniline and cyanamide and pyrolysed in N₂, from (22). Reprinted with permission from AAAS; (d) Fe-N-C catalyst prepared from a ferrous salt, phenanthroline and ZIF-8, and pyrolysed in argon (CNRS catalyst, transmission electron microscopy (TEM) image provided by Goran Drazic, National Institute of Chemistry, Slovenia)

Table I State-of-the-Art Oxygen Reduction Reaction Activity of Iron-Nitrogen-Carbon Cathode Catalysts in Single Cell PEMFC Measured under Pure Oxygen and Hydrogen^a

Current density at 0.9 V, mA cm ⁻²	Loading, mg _{Fe-N-C} cm ⁻²	Expected current density at 0.9 V at 5 mg _{Fe-N-C} cm ⁻² , mA cm ⁻²	Back pressure, bar	Cathode catalyst description	Ref.
5	4	6	1	Polyimide nanoparticles (NPs) (60 nm), multipyrolysis and leaching steps, final pyrolysis in NH ₃	(35)
7	1	35	1	Fe(II)salt + phen + ZIF-8, pyrolysis in argon at 1050°C then in NH ₃ at 950°C	(36)
3	1.5	10	1	Fe-porphyrin + Co-porphyrin + silica template, pyrolysed in N ₂ at 1000°C, HF leaching	(37)

Continued

Current density at 0.9 V, mA cm ⁻²	Loading, mg _{Fe-N-C} cm ⁻²	Expected current density at 0.9 V at 5 mg _{Fe-N-C} cm ⁻² , mA cm ⁻²	Back pressure, bar	Cathode catalyst description	Ref.
10	2	25	1	ZIF-8 + Fe elet rospun with polyac ylonitrile (PAN) and poly(methyl methac ylate (PMMA), pyrolysed at 1000°C in Ar then 900°C in NH ₃ , at d leab ed	(34)
4	4	5	0.5	Fe(II) salt + nie rbazin + silia template, pyrolysis in N ₂ , HF leab , pyrolysis in NH ₃	(38)
5	1	25	1	ZIF [Zn(eIm) ₂ rho] + Fe(II) + phen, single pyrolysis in NH ₃ at 950°C	(39)

^aPEMFC o nditions: 80°C, 100% RH feed gases, Pt/C anode

Large-transport across the cathode active layer (Figure 5). Oxygen transport limitation in a thick cathode is particularly exacerbated when it is fed with air (31, 34), which is the case for almost all PEMFC applications.

While the target in the early stage of non-pgm catalyst development extensively focused on the activity at high potential (volumetric activity or current density at 0.8 V or 0.9 V), the activity target is now accompanied by a power performance target

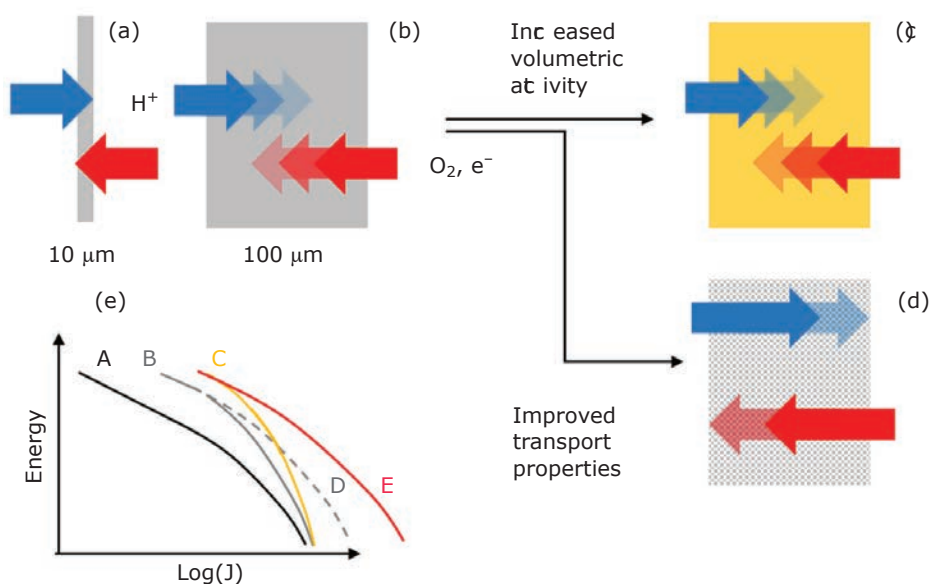


Fig. 5. Interplay between Fe-N-C cathode volumetric activity, thickness and transport properties in determining the cathode performance at low and high current densities: (a) thin Fe-N-C cathode (representative for 0.4 mg_{Fe-N-C} cm⁻²) with reference volumetric activity; (b) thick Fe-N-C cathode (representative for 4.0 mg_{Fe-N-C} cm⁻²) with reference volumetric activity; (c) thick Fe-N-C cathode with enhanced volumetric activity; (d) thick Fe-N-C cathode with reference volumetric activity but enhanced mass-transport properties; (e) next generation Fe-N-C cathode with improved volumetric activity and mass transport. The graph shows schemed Tafel plot presentations (potential vs. logarithm of the current density) of the cathode polarisation curves. The linear part corresponds to the current density region where the cathode is only controlled by ORR electrokinetics (no limitation by transport of O₂, protons and electrons)

(PEMFC operating point of typically 0.6–0.7 V) (see **Table II**). The volumetric activity of the Pt was specifically defined for non-pgm catalysts by the General Motors Fuel Cell group, USA, in 2003 (40). The volumetric activity is defined as the areal current density of a non-pgm anode normalised by the anode thickness ($A\ m^{-3}$, reported at 0.8 V or 0.9 V). As is valid for the Fe-N-C loading effect within certain conditions, the proportionality between current density of the cathode (when it is controlled by electrode kinetics) and anode thickness can be assumed to be valid within a certain range of thickness, Equation (i):

$$J\ (\text{at } 0.8 \text{ or } 0.9\ \text{V}) = j_v\ t \tag{i}$$

with J the current density ($A\ cm^{-2}$), j_v the volumetric activity (in $A\ m^{-3}$ at 0.8 V or 0.9 V) and t the anode thickness (m). As one can see, a possible approach to increase the current density at high potential may consist of increasing the thickness of the anode layer (**Figures 5(a)** and **5(b)**). From a cost perspective, this is feasible, but it faces practical limitations due to increasing average path lengths for O_2 , protons and electrons in order to reach the active sites. The opposite directions of the O_2 and protons flow can lead to particularly severe mass-transport limitations if they occur to form gradients of O_2 concentration and electrode potential, respectively (submerged as fading arrows in **Figure 5**). With current MEA technology, 100 μm is considered the upper realistic thickness limit for a Fe-N-C layer. This is already 10 times thicker than usual Pt-based anode layers (with a 50% Pt/C catalyst and a cathode loading of $0.4\ mg_{Pt}\ cm^{-2}$,

the electrode thickness is ca. 10 μm). The layer thickness for Pt/C and Fe-N-C catalysts alike is governed by the carbon loading, with apparent density of $0.37\text{--}0.40\ g_{carbon}\ from\ catalyst\ per\ m^3$ of electrode usually observed (30, 31, 40)). We extract from this a rule-of-thumb of 25 μm electrode thickness increment per $1\ mg\ m^{-2}$ of carbon material from the catalyst. Future efforts should thus focus on improving both the volumetric activity of Me-N-C catalysts and the mass-transport properties of Me-N-C layers (**Figures 5(c)** and **5(d)**, respectively), to ultimately combine advances in activity and transport properties to compete with Pt-based anode layers on the whole range of current density (**Figure 5(e)**, above E).

For Pt-based catalysts in contrast, there is no incentive to increase performance by increasing the Pt loading at the anode, because Pt is expensive. The trend is opposite, with attempts to reach break-even performance (same current density at a given cell voltage) but with lower Pt loading than today. The key parameter for pgm-based catalysts is the mass activity, i_M . Equation (ii):

$$J\ (\text{at } 0.9\ \text{V}) = i_M\ L \tag{ii}$$

with J the current density ($A\ m^{-2}$), i_M the mass activity (in $mA\ mg_{Pt}^{-1}$ at 0.9 V) and L the Pt loading at the anode ($mg_{Pt}\ m^{-2}$). Reporting the activity of pgm-based catalysts as a mass activity ($A\ g_{pgm}^{-1}$) and of non-pgm catalysts as a volumetric activity ($A\ m^{-3}$ anode) arises therefore from the different nature of the main limitations (cost for pgm-based anodes and performance for non-pgm anodes) (16). The targets set for non-pgm

Table II Non-pgm Cathode Current Density Targets at 0.9 V ('Activity') and 0.7 V ('Power Performance') in Single-Cell PEMFC (8)^a

Cathode feed	FCH 2 JU targets		US DOE targets	
	Experimental conditions	Current density at 0.9 V cell voltage	Experimental conditions	Current density at 0.9 V cell voltage
O ₂	H ₂ /O ₂ , 1 bar gauge/1 bar gauge, 80°C, 100% RH	75 mA m ⁻²	H ₂ /O ₂ , 0.5 bar gauge/0.5 bar gauge, 80°C, 100% RH	44 mA m ⁻² (8)
	Experimental conditions	Current density at 0.7 V cell voltage	–	–
Air	H ₂ /air, 2.5 bar gauge/2.3 bar gauge, 80°C, 50% RH/30% RH	600 mA m ⁻²	–	–

^aUS DOE target is equivalent to a Pt-cathode with mass activity of $44\ A\ g_{Pt}^{-1}$ at 0.9 V and a loading of $0.1\ mg_{Pt}\ m^{-2}$

talysts for automotive application in the recent FCH 2 JU action plan of 2017 (26) and that of the US DOE Office of Energy Efficiency & Renewable Energy (EERE) (27) are reported in Table II. By comparing Table I and Table II, one can see that today's most active Fe-N-C catalysts could reach, at a cathode loading of $5 \text{ mg}_{\text{Fe-N-C}} \text{ cm}^{-2}$, ca. one-third to half of the current density targets at 0.9 V set for the next generation of pgm-free catalysts.

While promising, sub-cathode layers should also show mass-transport properties appropriate to operation at high current density. Figure 6 shows representative examples of the best power performance single-cell PEMFC obtained with Fe-N-C cathodes and Pt-based anodes,

with the cathode fed with fully humidified O_2 (Figures 6(a)–6(c)) or fully humidified air (Figure 6(d)). At 0.6 V, the current density reaches $1.0\text{--}1.2 \text{ A cm}^{-2}$ in pure O_2 and the peak power density is nearly 1 W cm^{-2} at around $0.4\text{--}0.5 \text{ V}$ (Figures 5(a), 5(b) and 5(c)) (22, 31, 34). The use of a zinc-based zeolitic imidazolate metal-organic-framework (ZIF-8) as sacrificial precursor of carbon and nitrogen resulted in 2011 in a more open structure and higher accessibility to O_2 of the FeN_x sites formed during pyrolysis (Figure 5(a)) (31). Since then, ZIF-8 has been extensively studied for the preparation of highly microporous Fe-N-C and also N-C materials (41). Other metal organic frameworks (MOFs) have

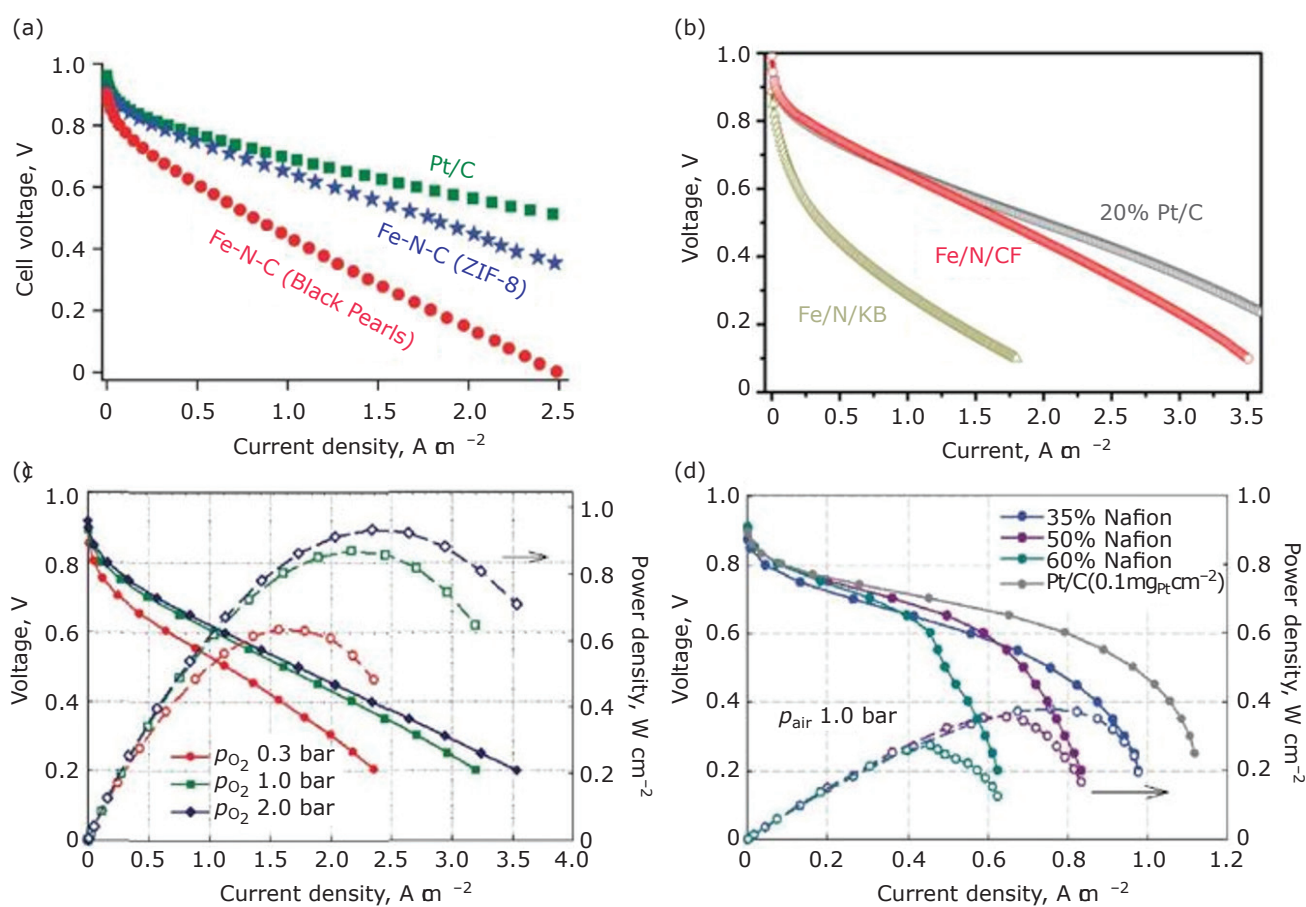


Fig. 6. Examples of state-of-the-art power performance obtained with Fe-N-C cathodes in single-cell PEMFC: (a) H_2/O_2 polarisation curve with a cathode prepared from ferrous acetate, phenanthroline and ZIF-8, pyrolysis in Ar then in NH_3 (blue curve), $3.9 \text{ mg}_{\text{Fe-N-C}} \text{ cm}^{-2}$ cathode, Pt-based anode, 80°C , 2 bar gas pressure on each side (0.5 bar is water vapour), the green curve is for a $0.4 \text{ mg}_{\text{Pt}} \text{ cm}^{-2}$ cathode (31); (b) H_2/O_2 polarisation curve with a cathode prepared by co-electrospinning $\text{Fe}(\text{phen})_3$ complex, ZIF-8 and polyacrylonitrile (labelled Fe/N/CF), pyrolysis in Ar then NH_3 (34), $3 \text{ mg}_{\text{Fe-N-C}} \text{ cm}^{-2}$ cathode, $0.3 \text{ mg}_{\text{Pt}} \text{ cm}^{-2}$ anode, 2 bar gas pressure on each side, 80°C , 100% relative humidity (RH); (c) H_2/O_2 polarisation curve with a cathode prepared from ferric salt, aniline and cyanamide, first pyrolysis in N_2 -acid-leaching-second pyrolysis in N_2 , $4 \text{ mg}_{\text{Fe-N-C}} \text{ cm}^{-2}$ cathode, $2 \text{ mg}_{\text{Pt}} \text{ cm}^{-2}$ anode, 80°C , dry O_2 partial pressure 0.3 bar, 1 bar or 2 bar (22); (d) H_2/air polarisation curve, dry air partial pressure 1 bar, 100% RH, otherwise same conditions as for (c). From (22). Reprinted with permission from AAAS

also been investigated, but Zn-based MOFs are so far the best candidates, and in particular the subcategory of ZIFs (39, 42, 43). The advantage of sub-ZIFs is the low boiling point of zinc (907°C). During the pyrolysis at $T > 950^\circ\text{C}$, most Zn (undesired in final Fe-N-C catalysts) is evacuated as volatile products while Fe stays. Avoiding excess Zn is thus avoidable. While high specific area and high microporous area in particular (pores with width ≤ 2 nm) are important for reaching high electrocatalytic activity with Fe-N-C catalysts (22, 30, 44), the connection between micropore-hosted FeN_x moieties and the macroporous structure of the electrode is an important key for proper accessibility by O_2 . Mesoporosity can be introduced during the catalyst synthesis preparation (for example, with a silica template approach or pore-forming agents (38, 45, 46)), but macroporosity often depends on the electrode preparation method as a whole, not only on intrinsic catalyst morphology (47). An original approach to combine the microporosity of ZIF-8 derived Fe-N-C catalyst with macroporosity in the electrode resorted to the electrospinning of Fe-doped ZIF-8 with a carrier polymer (34). The carrier polymer forms fibrous structures, imparting inter-fibre macroporosity in the final electrode structure. Another broad approach for the synthesis of highly active Fe-N-C catalysts has involved the use of sacrificial monomers or polymers as C and N sources (48, 49). **Figure 5(c)** shows the H_2/O_2 polarisation curve with Fe-N-C cathode prepared from the pyrolysis of an iron salt and two different monomers, aniline and γ -anamide. The two different monomers helped in forming a bimodal porosity, with the addition of γ -anamide increasing greatly the microporous surface area in the final Fe-N-C catalyst (22).

While the beginning-of-life H_2/O_2 polarisation curves of single-cell PEMFC comprising Fe-N-C cathodes now approach those of Pt/C cathodes, the performance in H_2/air conditions (needed for use in technologically-relevant conditions) is facing severe mass-transport issues. **Figures 6(c)** and **6(d)** show the effect, for a same Fe-N-C cathode, of switching from pure O_2 to air. The power density is reduced by a factor >2 , and the polarisation curves on air are characterised by a strong bending above ca. 0.4 A cm^{-2} . This bending occurs at lower current densities than when using Pt/C cathodes, likely due to a much greater thickness of Fe-N-C cathodes at a loading of $4 \text{ mg}_{\text{Fe-N-C}} \text{ cm}^{-2}$, relative to Pt/C cathodes of typically $0.4 \text{ mg}_{\text{Pt}} \text{ cm}^{-2}$ ($0.6 \text{ g}_{\text{carbon}} \text{ cm}^{-2}$, assuming a typical 40% Pt/C catalyst). Such Fe-N-C cathodes

are typically about 80–100 μm thick while Pt/C cathode thickness is $\leq 20 \mu\text{m}$.

Another practical advantage of pgm-free Me-N-C cathode catalysts is their strong resistance to poisoning, while Pt-based catalysts suffer from severe poisoning from various species, including some gases that can be present at trace amounts in fossil-derived H_2 (**Figure 7**) (50) but also anions, including chloride anions that are commonly encountered in field applications.

In summary, further improvement of the performance of Me-N-C cathode layers in PEMFCs can be reached by either increasing the catalyst activity (the cathode can then be made thinner, while preserving the 'apparent' cathode activity) or by increasing the reactant transport properties of the cathode layer, including long-distance transport (through the porous cathode) and short-distance transport (which can be modulated by catalyst morphology or agglomerate size). The major experimental efforts have hitherto focused on increasing the ORR activity of Me-N-C materials. Subsequent efforts are still critical to further increase the activity, selectivity and durability of sub-catalysts, but work on cathode layer design and catalyst morphology is also critical to improve non-pgm cathode behaviour at high current density when fed with air.

2.3 Deconvoluting Activity of Me-N-C Catalysts into Site Density and Turnover Frequency

If 100–125 μm remains the upper limit of practical Me-N-C layer thickness in the future, then further increasing the current density at 0.9 V will require increasing the volumetric activity. This can mainly be achieved via increasing either the number of active sites per unit volume (site density, SD, i.e. the number of sites that can be electrochemically addressed) or the specific activity for ORR (turnover frequency, TOF) of single sites, Equation (iii):

$$j_V (\text{at } 0.8 \text{ or } 0.9 \text{ V}) = \text{SD TOF}_{(\text{at } 0.8 \text{ or } 0.9 \text{ V})} e \quad (\text{iii})$$

where SD has units of sites m^{-3} , TOF has units of electrons $\text{site}^{-1} \text{ s}^{-1}$ and e is the electroic charge of one electron (C electron^{-1}). On one hand, increasing the wt% Pt on a support (typically, carbon powder) nearly proportionally increases the apparent activity of the Pt-supported catalyst. Pt nanoparticles of 2–3 nm size can now be grown on carbon supports up to ca. 50 wt% Pt on carbon (51) before the average Pt particle size

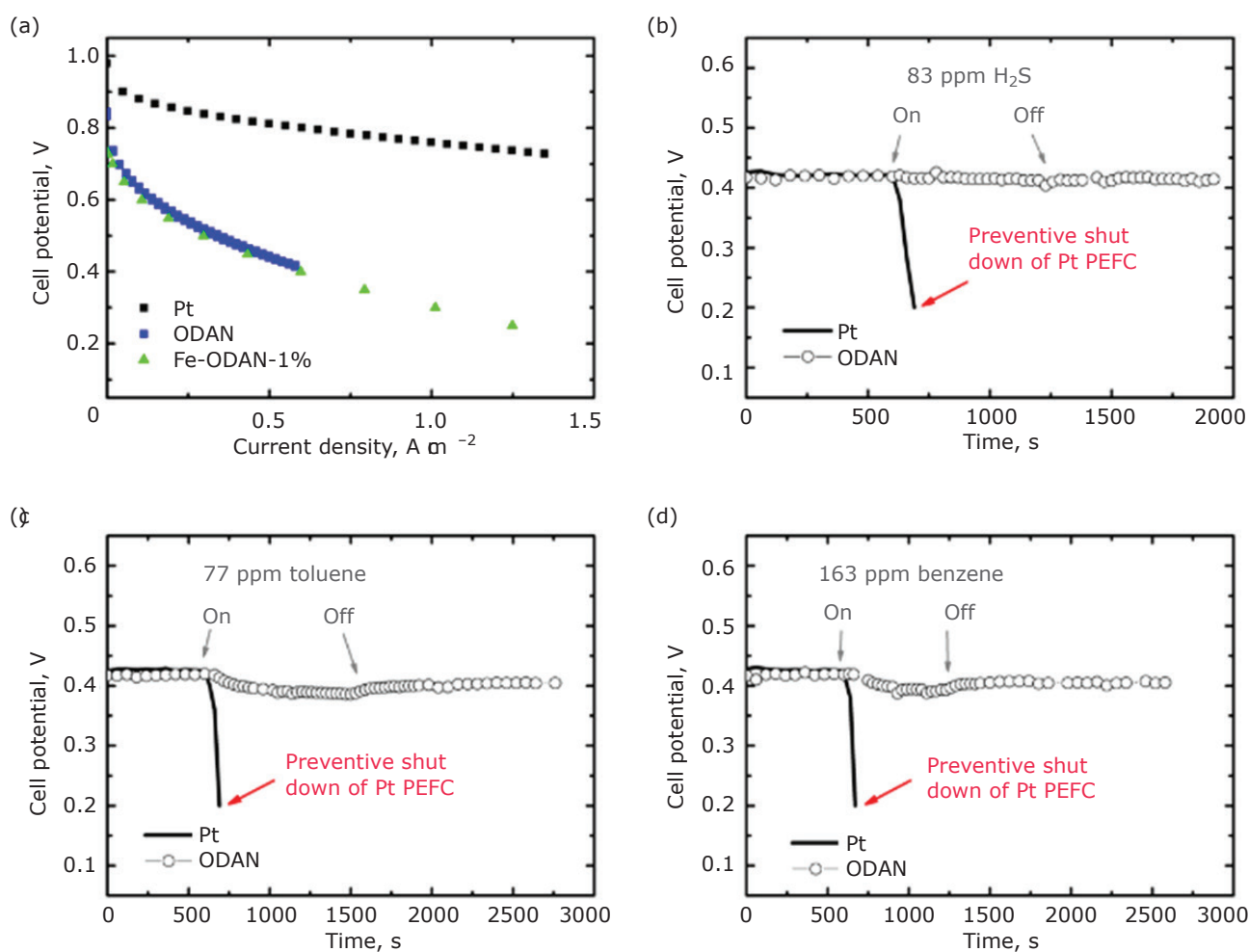


Fig. 7. (a) H₂-O₂ polarisation curve for an MEA comprising either a Fe-N-C cathode (4 mg cm⁻² loading) or a Pt/C cathode (0.4 mg_{Pt} cm⁻²); cell voltage before and after addition of: (b) 83 ppm H₂S; (c) 77 ppm toluene; and (d) 163 ppm benzene in the cathode gas stream. Reproduced with permission from (50). Published by the Royal Society of Chemistry

significantly increases. This allows high Pt mass and Pt surface area per volume of electrode to be realised. As a consequence, Pt-based cathodes are highly active but at the same time relatively thin (5–15 μm), which secures high accessibility by O₂, protons and electrons. For pyrolysed Fe-N-C or Co-N-C catalysts, the situation is different. While the metal atoms are atomically dispersed as Me-N_x moieties at low metal content (up to ca. 3 wt% metal (Fe or Co) on N-C, as is the case for the catalysts of Figure 4), at higher metal contents the metal atoms aggregate during pyrolysis to form reduced metallic particles or metal carbides. Subcrystalline structures are often partially or totally surrounded by graphitic shells during pyrolysis, which protects them somewhat from the acidic environment during electrochemistry. While sub-core-shell Metal-N-C structures may have some

ORR activity in acidic medium, many observations show that their intrinsic activity is much less than that of the atomically dispersed Me-N_x moieties (52). As a consequence, Me-N-C catalysts display a much lower weight content (<5 wt%) of active metal relative to Pt/C catalysts (50 wt%). From a given supposed wt% of potentially active metal in Me-N-C material (MeN_x moieties in the bulk or on the surface), the atomic mass and the utilisation factor (ratio of electrochemically addressable MeN_x moieties to total number of moieties in a given catalyst), it is possible to calculate expected SD values. Table III shows that only a slightly lower SD-value is calculated for Fe-N-C (3 wt% Fe) vs. 50 wt% Pt/C catalyst if one assumes that the site utilisation of Fe-N_x moieties is 100%. Also of practical interest, it in turn implies that the loading of FeN_x sites per m² of MEA is only four times

Table III Examples of Site Density and Site Loading Numbers for Iron-Nitrogen-Carbon and Platinum on Carbon Catalysts for Oxygen Reduction Reaction as well as $\text{Ni}(\text{P}_2\text{RN}_2\text{R}')^{n+}$
a, b, c

Catalyst description	SD, number of sites per cm^3 of electrode	SL, number of sites per cm^2 electrode	Corresponding catalyst loading, mg cm^{-2}
Fe-N-C, 3 wt% Fe, 100% site utilisation	1.29×10^{20}	1.29×10^{18} ^d	$4 \text{ mg}_{\text{Fe-N-C}} \text{ m}^{-2}$ ^d
Fe-N-C, 3 wt% Fe, 25% site utilisation	3.23×10^{19}	3.23×10^{17} ^d	$4 \text{ mg}_{\text{Fe-N-C}} \text{ m}^{-2}$ ^d
Pt/C, 50 wt% Pt, 25% site utilisation ^c	3.09×10^{20}	3.09×10^{17} ^e	$0.4 \text{ mg}_{\text{Pt}} \text{ m}^{-2}$ ^e
$[\text{Ni}(\text{P}_2\text{RN}_2\text{R}')_2]^{n+}$, 100% site utilisation, (53)	7.5×10^{18}	1.5×10^{16} ^f	$0.04 \text{ mg}_{\text{NiP}_2\text{N}_2} \text{ m}^{-2}$ ^f
Pt/C 50 wt% Pt, 25% site utilisation	3.9×10^{19}	3.9×10^{16}	$0.05 \text{ mg}_{\text{Pt}} \text{ m}^{-2}$

^aThe amount of electrochemically addressable active sites in $\text{Ni}(\text{P}_2\text{RN}_2\text{R}')^{n+}$ was determined from cyclic voltammetry

^bUltra-low loading of Pt/C for HOR. The value of $0.4 \text{ g}_{\text{carbon}} \text{ per m}^3$ of electrode volume was assumed for all catalysts. For Fe-N-C, it was assumed that either 100% or 25% of the Fe-N_x moieties are surface-exposed (participate in the ORR), while for Pt/C, it was assumed that $\frac{1}{4}$ of the Pt atoms are surface-exposed (ratio corresponding to Pt particles of ca. 2–3 nm)

^cThis Pt site utilisation expresses only the ratio of surface Pt atoms to all Pt atoms. We highlight however that not all Pt surface sites are equivalent in terms of TOF, with terrace sites and on-edge coordinated Pt sites being more active for ORR (54, 55)

^dFor a 100 μm -thick electrode

^eFor a 10 μm -thick electrode

^fFor a 25 μm -thick electrode

higher for a 100 μm thick Fe-N-C anode than for a 10 μm thick Pt/C anode (Table III). Thus, as a result of combined constraints in anode layer thickness and in active metal content in pyrolysed Fe-N-C catalysts, these straightforward calculations imply that, in order to reach a same current density at 0.8 V or 0.9 V, such a Fe-N-C anode must comprise FeN_x active sites with a TOF that is in fact very comparable to that of surface-exposed Pt atoms. Table III also reports the numbers calculated assuming that only $\frac{1}{4}$ of the Fe-N_x moieties are utilised (on the surface). The assumed utilisation factor of 0.25 is in line with very recent quantifications of site utilisation for such materials (see later).

Some possible pathways toward increased activity of Me-N-C catalysts are schemed in Figure 8, reached via increasing either the SD or TOF (Equation (iii)). While increasing the metal content without formation of metallic particles during pyrolysis may remain limited, there might be some gain possible relative to the present status (see Figure 4). Increased density of defects in graphene sheets (in-plane sites) or increased edge length per mass of carbon (edge sites) could allow increase of the density of FeN_x active sites (step B in Figure 8). At a fixed bulk metal content, preferential formation of FeN_x sites on the surface of the carbon material,

rather than statistical distribution on the surface and in the bulk, could increase the utilisation factor of FeN_x sites (in electrocatalysis, only the sites at the solid-electrolyte interface are electrochemically active) (step C in Figure 8). The utilisation factor of statistically-dispersed FeN_x moieties could also be increased via increased carbon surface area (decreased average number of stacked graphene sheets in the material, step D in Figure 8). The TOF of single metal-atoms in MeN_x moieties might also be increased, either through the preferential formation of certain MeN_x moieties (for example edge vs. in-plane, if edge defects are more active, or vice versa if in-plane defects are shown to be more active) or the formation of more complex sites. One sub possibility is the formation of binuclear Fe_2N_x sites, where the Fe-Fe distance is commensurate with the O=O bond distance, allowing the two Fe centres to work faster than two individual FeN_x moieties (32). Other additional parameters have been proposed or investigated to tune the TOF, such as bi-metallic catalysts (for example Fe-Mn or Fe-Co) (56, 57), and *d*-doped carbon by nitrogen and another light element (such as sulfur, phosphorus or boron) (58). The introduction of bimetallic elements other than Fe(Co), N and C could indeed offer broader perspectives on the electrocatalytic properties of the graphene sheets, and thereby of

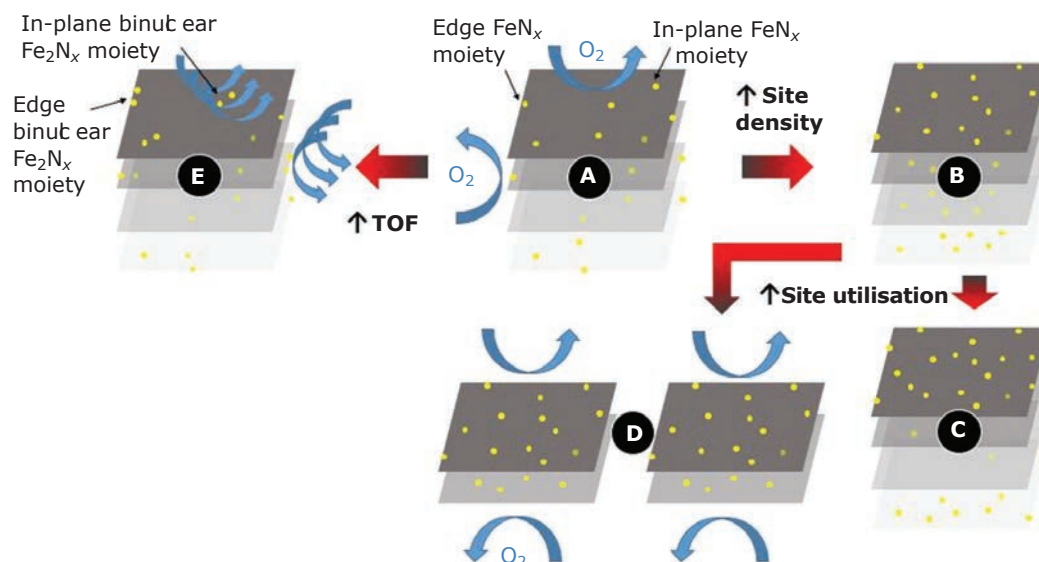


Fig. 8. Scheme of possible ways to increase the volumetric activity of Me-N-C catalysts: **A** typical Fe-N-C catalyst with four stacked graphene sheets including in-plane and edge FeN_x sites. Only the FeN_x sites on the top and bottom sheets are O_2 accessible; **B** Fe-N-C catalyst with higher Fe content, including O_2 -accessible and O_2 inaccessible sites; **C** Fe-N-C catalyst with preferential location of FeN_x sites on the top and bottom graphene sheets (O_2 -accessible surfaces); **D** Fe-N-C catalyst with higher specific surface area (lower number of stacked graphene sheets); **E** Fe-N-C catalyst featuring binuclear Fe_2N_x sites with possible cooperative $\text{O}=\text{O}$ bond dissociation on the two Fe centres

the electron density at the Fe centres (59). The O_2 binding energy and therefore the TOF might be increased further with one of those approaches.

Whether the MeN_x sites are mostly located in-plane or on the edge of graphene or disordered graphene sheets is important (22, 23, 30, 60, 61). Answering that question would indicate whether the in-plane size of graphene sheets must be decreased or the average number of stacked layers decreased. For a set of Fe-N-C catalysts prepared via the silica template method and using niobiazin and iron nitrate as N, C and Fe precursors, it was shown that decreased stacking led to increased activity, implying that most of the active sites are in-plane moieties for this synthesis (Figure 9) (60). Interestingly, the carbon matrix was highly graphitic for this set of catalysts (60), in contrast with what is usually observed on most Fe-N-C catalysts that are highly ORR-active (31, 62–64). The average number of stacked graphene layers is typically only 4–6, as estimated from Raman spectroscopy, for high-surface-area amorphous carbon structures in Fe-N-C catalysts. Formation of large in-plane voids (several carbon atoms removed, see for example Figure 4(b)) could also allow O_2 access to in-plane FeN_x moieties that are not situated in the uppermost graphene layer of a graphitic crystallite,

thereby breaking the relationship between stacking number and ORR activity. Such a relationship is otherwise expected, with the hypothesis that most FeN_x sites are located in-plane.

In guiding experimental efforts, disentangling the overall volumetric activity into SD and TOF (Equation (iii)) is not only of scientific importance but also has technological implications on the development of promising catalyst preparation routes and on the design of high-performance non-pgm cathode layers. For example, a low SD-value implies stringent requirements on local mass-transport properties near active sites, for a given current density of the cathode layer. One method is developed for quantifying SD in Me-N-C catalysts, TOF values can then be deduced from the combined knowledge of the experimental values of activity and SD. As an example, TOF values much higher than that of surface-located Pt atoms in Pt/C catalysts may lead to additional mass-transport issues at short range (higher local diffusion flux of O_2 needed towards individual active sites). In addition, Me-N-C catalysts with high TOF but low SD may not only lead to local O_2 starvation when operating at high current density in PEMFC, but may also lead to the build-up of hydrogen peroxide concentration gradients

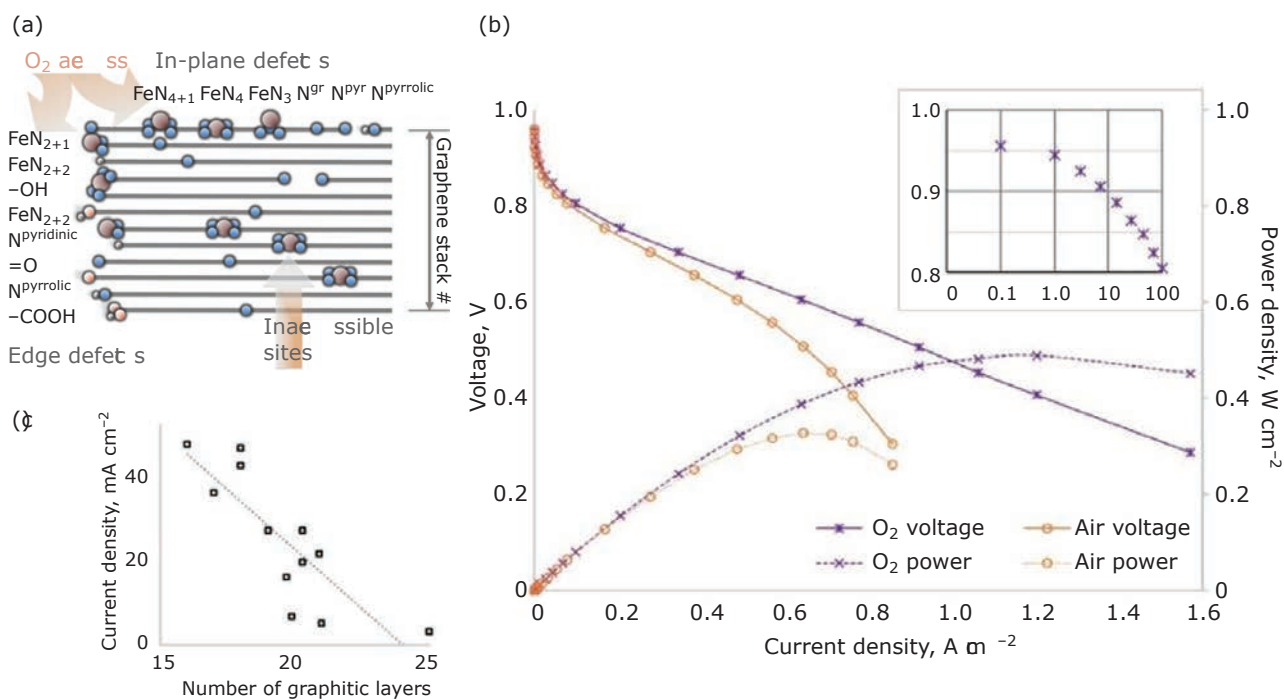


Fig. 9. Effect of average number of stacked graphene sheets on ORR activity of pyrolysed Fe-N-C catalyst: (a) Scheme of in-plane and edge FeN_x sites and O₂ (in)accessibility; (b) PEMFC polarisation curves with H₂/O₂ or H₂/air feed; (c) negative correlation between current density at 0.8 V read on the H₂/air polarisation curve and the average number of stacked graphene layers for a set of 12 Fe-N-C catalysts. Test conditions: 80°C, 100% RH, 1.5 bar (H₂/O₂) and 2.5 bar (H₂/air) total gas pressures. Reprinted with permission from (60). Copyright (2017) American Chemical Society

(high oxygen concentration locally around active sites), with expected dramatic influence on the long term durability of Me-N-C cathodes (65). For all these reasons, disentangling SD and TOF values from the overall ORR activity will be important for the further development of Me-N-C catalysts.

Whereas established methods exist for Pt-based catalysts (carbon monoxide chemisorption, electrochemical hydrogen sorption) they do not work at room temperature for Me-N-C catalysts. Reliable quantification of the catalytic sites on the surface of pyrolysed Me-N-C catalysts is an ongoing challenge. Attempts have been made in the past to estimate the values of SD and TOF of some Fe-N-C catalysts (66, 67), however those estimations have always included one or more hypotheses such as: (a) full utilisation of all Fe atoms in Fe-N-C ($\text{Number}_{\text{Fe}} \text{ m}^{-3} = \text{SD}$); or (b) full utilisation of the FeN_x moieties (a less credible hypothesis than (a), but still probably far from the real Fe utilisation). ⁵⁷Fe Mössbauer spectroscopy is powerful in distinguishing FeN_x moieties from crystalline Fe structures. Even though clean Fe-N-C catalysts with an ⁵⁷Fe Mössbauer spectroscopic signature showing only quadrupole doublets (assigned to atomically

dispersed Fe-ions) can now be synthesised, the fact that Mössbauer spectroscopy is a bulk technique implies that it cannot directly distinguish bulk sites from surface sites. The same observation applies to X-ray absorption spectroscopy, the other broadly applied technique to characterise the local environment around Fe and Co centres in pyrolysed Me-N-C catalysts. Recent years have witnessed the development of a few *ex situ* (gas-solid) and *in situ* (liquid-solid) sorption techniques to assess the SD of sub-nanometre catalysts. These rely on the strong interaction of a small probe molecule with surface adsorption sites resulting in poisoning of the site.

Early non-pgm catalyst poisoning studies realised that CO_{gas}, an intuitive choice of poison for Fe centres, is unable to block Fe-N-C sites quantitatively under ambient temperature and pressure conditions (68, 69). In contrast, the cyanide ion was identified as a suitable *in situ* poisoning ligand for FeN₄ centres (70, 71). Owing to its irreversible adsorption however, CN⁻ adsorption could not be utilised for quantitative SD evaluation. Recently, an *ex situ* low-temperature (-100°C) CO gas pulse chemisorption-based technique for the quantification of the SD of Fe-Mn-N-C and Mn-N-C catalysts was reported

by Strasser's group (**Figures 10(a)** and **10(b)**). Quantitative values of SD were directly obtained from the total amount of adsorbed CO derived from consecutive CO pulses (72). Subsequent thermal desorption of the adsorbed CO during heating ramps from -100°C to about $+400^{\circ}\text{C}$ provided additional insight on the desorption kinetics and, indirectly, into the relative CO chemisorption energies of different FeN_x or dissimilar Me-N_x sites. This SD estimation technique is straightforward, robust and may be applicable to various non-pgm metal centres. Its drawback consists of the fact that it is performed

outside the electrolyte, and thus relies on the assumption that all sites probed by gas molecules remain active and accessible in an electrochemical environment. More recently still, an electrochemical *in situ* technique to probe, evaluate and quantify the SD at the surface of a powder catalyst electrode was reported by Kucernak's group (73). The authors demonstrated a protocol that allows the quantification of SD in Me-N-C catalysts operating under acidic conditions by means of nitrite adsorption, followed by reductive stripping (**Figures 10(c)** and **10(d)**). The method showed direct correlation to the catalytic

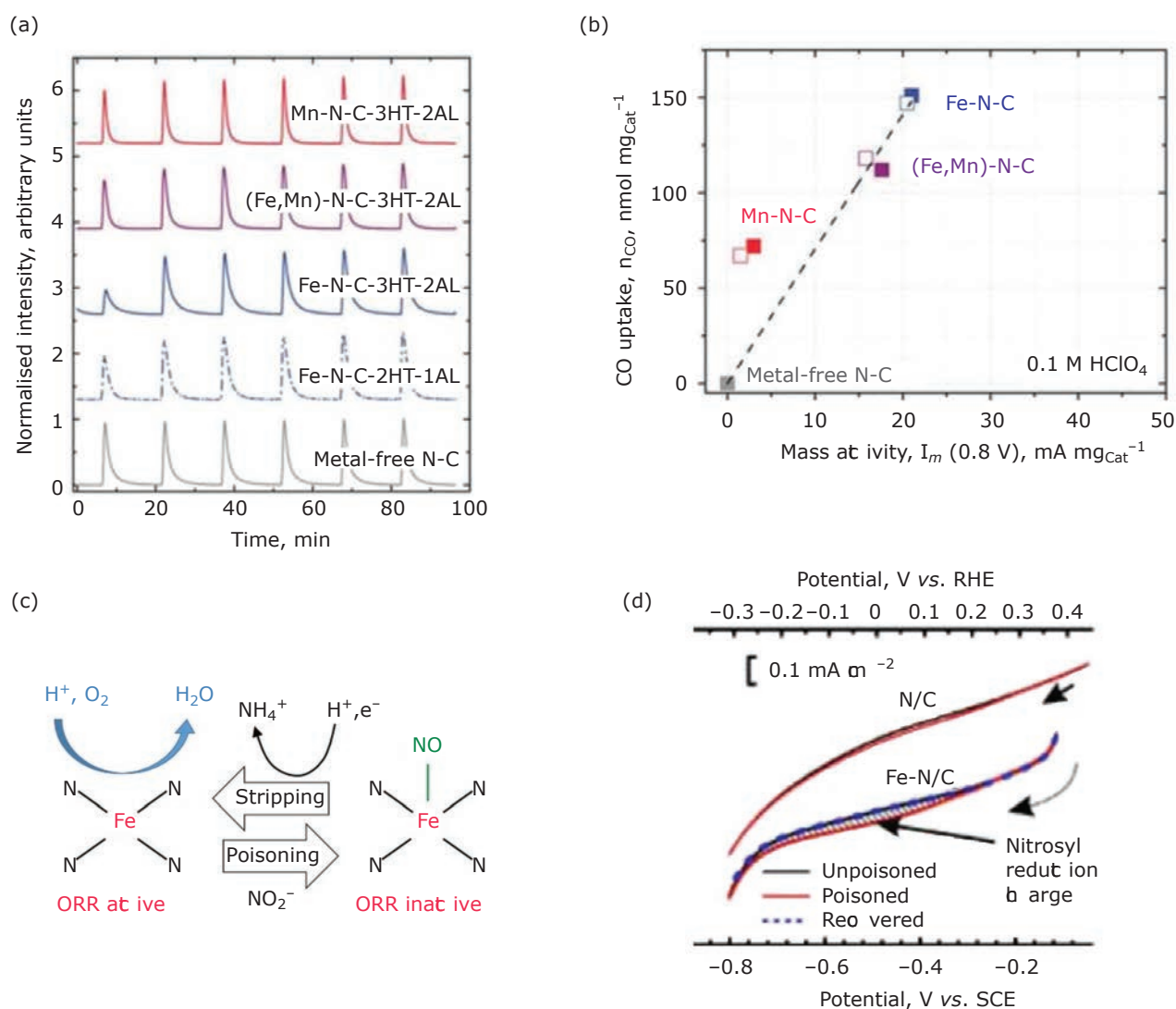


Fig. 10. Scheme of methods recently developed to quantify SD in pgm-free cathode catalysts: (a) quantification of moles CO adsorbed on monometallic Fe-N-C and Mn-N-C materials, or bimetallic Fe-Mn-N-C materials (labelled as (Fe,Mn)-N-C, although not necessarily implying binuclear active sites) by pulsed CO chemisorption at low temperature; (b) correlation between CO uptake (mole per $\text{mg}_{\text{catalyst}}$) and ORR activity; (c) scheme showing the poisoning of Fe site by nitrite leading to stable Fe-NO adducts and its removal by reductive stripping, leading to the regeneration of the ORR-active Fe site; (d) the number of Fe sites is determined from the electric charge associated with Fe-NO adducts during electrochemical reduction. Reproduced from (72) and (73)

activity and was demonstrated for a number of non-pgm catalyst materials. Lastly, a recent study from Los Alamos National Laboratory showed that a specific doublet in the Mössbauer spectrum of an Fe-N-C catalyst was modified in the presence of NO (74). After an electrochemical reduction treatment applied to convert potential Fe^{III}N₄ moieties into Fe^{II}N₄ moieties, the introduction of NO-gas strongly modified only one doublet. That doublet accounted for 24% of the relative absorption area while the sum of all doublets (all types of FeN_x moieties) accounted for 63% of the absorption area. This defines a utilisation factor of 0.38 for that specific catalyst, in line with the expected utilisation factor if FeN_x moieties are statistically dispersed in graphene sheets, and with an average stacking (as determined experimentally) of five graphene sheets.

In the near future, one or several of these methods and possibly new ones will eventually be regularly applied by research groups in the field. This will give more detailed information on both the SD and TOF values in sub-catalysts and will guide the design of sub-catalysts and catalyst layers (Figure 11). Sub-methods that allow deconvolution of SD and TOF values will also inform on how these values change after various electrochemical or thermal aging of the catalysts. This will lead to novel understanding in particular

on whether the main instability (decreased ORR activity over time) of pgm-free Me-N-C catalysts in PEMFC mostly originates from a decreasing SD or from a decreasing average TOF over time.

3. Non-pgm Anode Catalysts

3.1 Limitations of Platinum Catalysts

The anode Pt loading in PEMFC is currently around 0.05 mg cm⁻² and cannot be further decreased without unacceptably increasing the anode sensitivity to H₂-fuel contaminants. Indeed in floating electrode configuration, Pt nanoparticles supported on carbon black (20–50 wt% Pt/C) at ultra-low loadings <5 μg_{Pt} cm⁻² have shown HOR exchange current density of 100 mA cm_{Pt}⁻² (80 A mg_{Pt}⁻¹ ‘mass-normalised’ exchange current density) at room temperature, with the performance doubling when the temperature is increased to 60°C (75). However, ultra-low loaded Pt catalyst layers (1–5 μg_{Pt} cm⁻²) are extremely sensitive to a range of contaminants (CO, hydrogen sulfide) present in the fuel or leached from stack components that reversibly or irreversibly deteriorate their activity. Hence, the design of catalysts with ultra-low Pt content that are more tolerant to contaminants, or of non-Pt HOR catalysts that are immune to

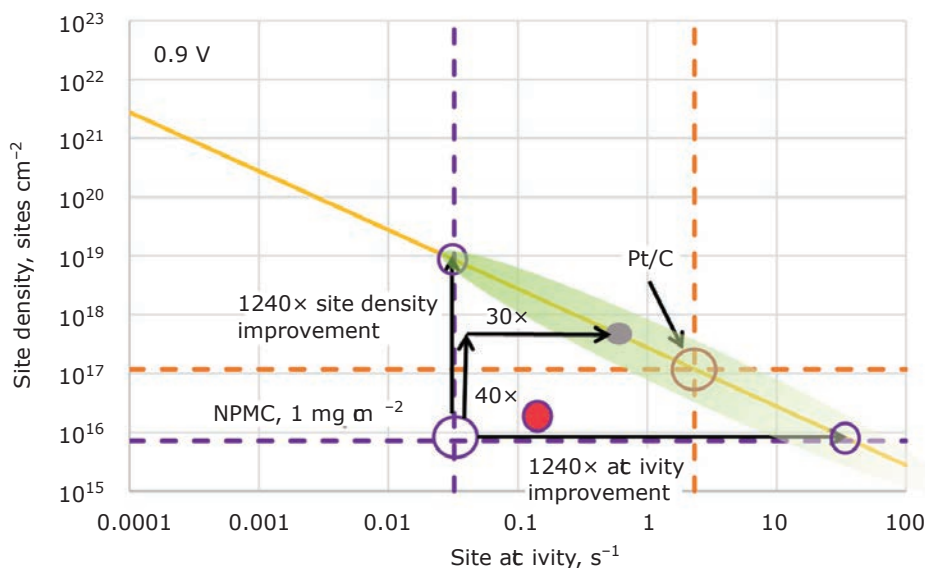


Fig. 11. Master plot showing the linear relation between site loading (number of active sites per cm² geometric area of cathode) and site TOF (number of electrons reduced per site and per second, at 0.9 V). The orange line corresponds to an iso-activity curve of 44 mA cm⁻² at 0.9 V for the cathode (US DOE target for O₂-fed cathode, see Table II), which can be reached with different combinations of SL and TOF values. The SL value is itself a combination of the SD and cathode thickness. The operating point for Pt nanoparticles on carbon is indicated with the orange circle. Two Fe-N-C cathodes with loading of 1 mg_{Fe-N-C} cm⁻² are represented (open purple circles and filled red circle) as well as three possible paths to reach the cathode activity target, for a fixed cathode thickness

o ntaminants would not only further reduce the total Pt content in PEMFCs but would also facilitate the use of lower cost H₂ reformed from natural gas or produced from biomass. This would ease the transition between 'fossil' H₂ and renewable H₂.

3.2 Tungsten and Molybdenum Carbides

Except for pgms, nickel as well as several Ni-alloys can drive HOR catalysis in highly alkaline conditions (76). For a long time, tungsten and molybdenum carbides possibly doped with Co or Ni (WC, M/WC, M = Ni, Co and Co/MoC) were the only pgm-free HOR catalysts that are stable under acidic conditions (77–79). Anodes based on these materials mixed with carbon black have exhibited current densities up to 20–40 mA cm⁻² at 0.1 V vs. reversible hydrogen electrode (RHE) (77–79). Such materials have proven quite resistant to CO (80) and have been successfully implemented as MEA anodes together with Pt-based cathodes and displayed a maximum power density of ~20 mW cm⁻². The replacement of Pt by such catalysts in single-cell PEMFC has so far resulted in a factor-10 lower power density (Figure 12) (81). However, they suffer from limited activity and also limited stability due to carbide oxidation (and release of CO₂) coupled to the formation of the corresponding metal oxides.

3.3 Bioinspired Nickel-Diphosphine Catalysts

More recently, a bioinspired approach for pgm-free HOR catalysts was developed. Hydrogenases are

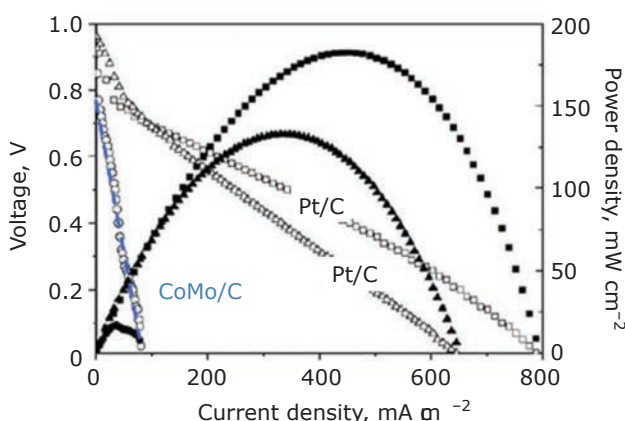


Fig. 12. Fuel cell polarisation curves with a typical Pt/C catalyst at the cathode and, at the anode, Co-Mo carbide or Pt/C. Reproduced from (81) with permission from Elsevier

enzymes that reversibly catalyse HOR to use the equilibrium potential and with turnover frequencies exceeding 1000 s⁻¹ for both HOR and HER at 0.2 V overpotential (82). Hydrogenases only contain Ni and metal atoms in a sulfur-rich and organometallic environment at their active sites (Figure 13) (83, 84). Inspired by the structure of these active sites, [Ni(P₂^RN₂^{R'})₂]ⁿ⁺ catalysts based on a nickel(II) centre coordinated to two diphosphine ligands, and bearing two pendant amine groups in a distorted square-planar geometry were designed by DuBois (Figure 13) (85, 86). Sub amine groups mimicking the pendant base found at the [FeFe]-hydrogenase active site act as proton relays in close proximity to the metal-bound hydride to promote H–H bond formation during the hydrogen evolution reaction (HER), and as a polariser of the H–H bond, to promote its cleavage during HOR (87, 88). Bioinspired [Ni(P₂^RN₂^{R'})₂]ⁿ⁺ complexes display bidirectional activity in HER and HOR with a few derivatives being reversible HER/HOR catalysts, albeit with a kinetic bias towards one or other direction (89–92). Almost reversible HER/HOR catalysis is observed in fully aqueous electrolyte with [Ni(P₂^{Cy}N₂^{Arg})₂]⁷⁺, although at elevated temperatures (91). Maximal HOR TOFs have been reported in the range of 10² s⁻¹ at pH values between 0 and 1, with dramatic decrease as soon as the pH exceeds 2.

Immobilisation of [Ni(P₂^RN₂^{R'})₂]ⁿ⁺ complexes on carbon nanotubes (CNTs) deposited onto gas diffusion layers (GDL) yields very efficient reversible catalytic materials for HER/HOR (93–95). Three distinct immobilisation modes (σ valent, π-stacking and electrostatic) have been developed to attach the bioinspired catalytic site onto subnanostructured electrodes (96). To that aim, various [Ni(P₂^RN₂^{R'})₂]ⁿ⁺ structures incorporating distinct anchoring groups were used. Figure 13 shows the structure of [Ni(P₂^{Cy}N₂^{Arg})₂]⁷⁺, [Ni(P₂^{Cy}N₂^{Ester})₂]²⁺ and [Ni(P₂^{Cy}N₂^{Py})₂]²⁺ containing arginine, activated ester and pyrene anchoring groups, respectively. With different anchoring groups on the molecular catalyst or different anchoring groups on the CNTs (Figure 13(b)). Standard grafting strategies were employed: polyanionic polyanionic electrostatic interaction (95), σ valent amide linkage (94) and π-stacking of a pyrene moiety directly onto CNTs (93). An alternative procedure was developed to construct molecular [Ni(P₂^RN₂^{R'})₂]ⁿ⁺ catalytic sites in a stepwise manner on the CNT-based electrode (53), in which the diphosphine ligand was firstly immobilised *via* amide coupling and the nickel

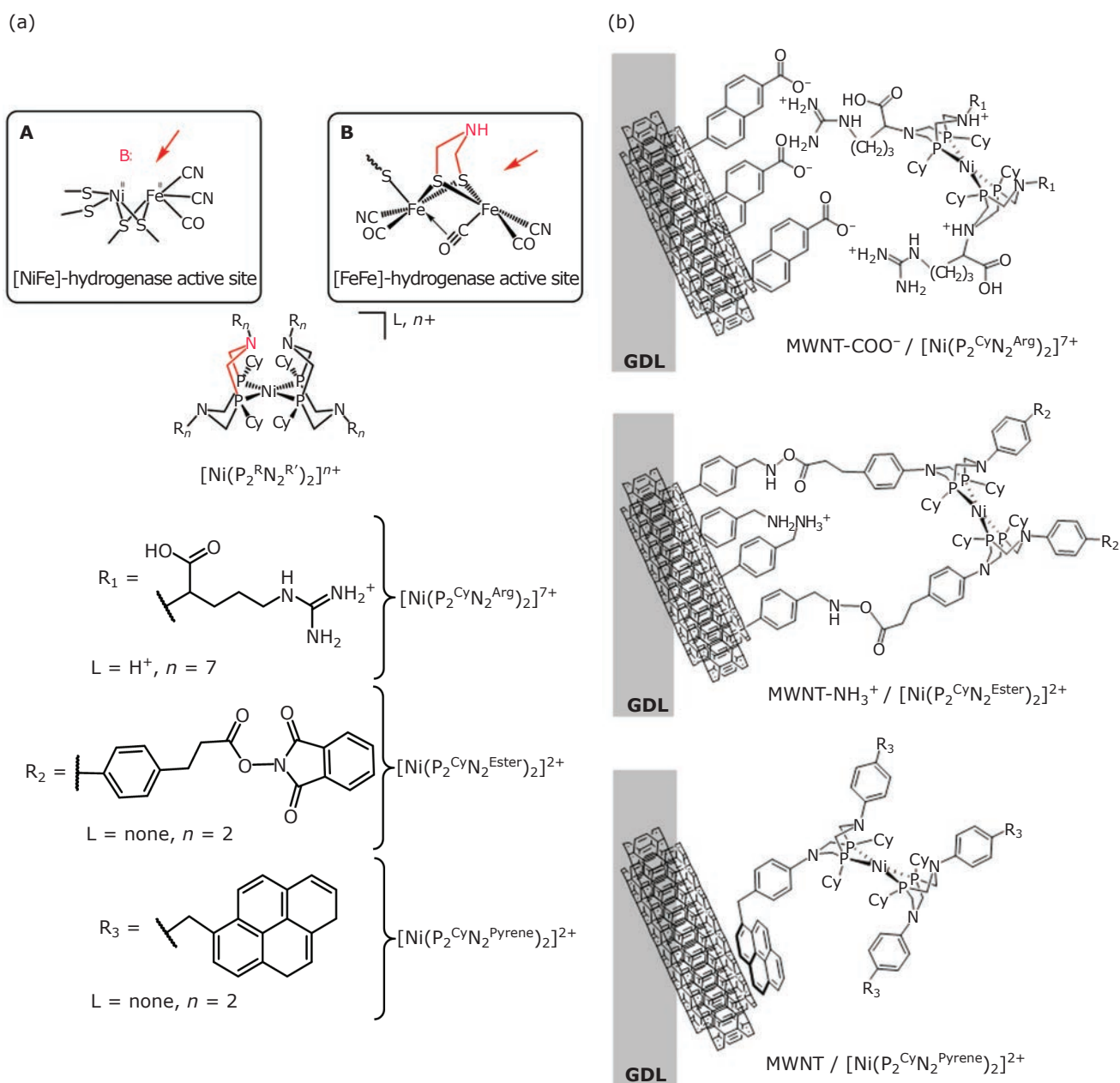


Fig. 13. (a) Three molecular complexes for H₂ oxidation and evolution with anchoring groups, inspired from the active sites of [FeFe]-hydrogenases. Here, the active site of *C. reinhardtii* HydA (**B**) is represented in its native state and a H₂ molecule can coordinate where the red arrow points (83). The NiFe active site of *E. coli* Hyd1 is represented in a similar fashion (**A**) (84); (b) three bio-inspired molecularly-engineered nanomaterials for H₂ oxidation: MWNT-COO⁻/[Ni(P₂^{CyN₂^{Arg})₂]⁷⁺, MWNT-NH₃⁺/[Ni(P₂^{CyN₂^{Ester})₂]²⁺ and MWNT/[Ni(P₂^{CyN₂^{Pyrene})₂]²⁺. Adapted from (96) with permission of the Royal Society of Chemistry}}}

entre was then introduced in a second step in the form of a commercially available nickel salt (97).

Electrochemical characterisation of the final electrodes in acetonitrile allowed quantification of the amount of [Ni(P₂^{RN₂^{R'})₂]ⁿ⁺ species that are electrochemically addressable and display a two-electron wave in cyclic voltammetry. In brief, all techniques provide typical site densities (number}

of sites per geometric area of electrode) of 1–3 × 10⁻⁹ mol m⁻² when densely packed CNT electrodes are used. This loading is increased by one order of magnitude when carbon microfibres are used as templates to provide the CNT electrodes with three-dimensional structuring. This value (2 × 10⁻⁸ mol m⁻²) was used to determine SD and site loading (SL) data in **Table III** (53).

The electrocatalytic activity of all these materials was first assessed in 0.5 M sulfuric acid aqueous solution in a nitrogen or H₂ atmosphere provided from the back of the porous substrate in half-cell configuration (floating electrode technique, **Figure 14**). In some cases, the [Ni(P₂^RN₂^{R'})₂]ⁿ⁺-coated electrodes were coated with a Nafion membrane to form a stable, ppm-free, air-resistant MEA. Under such conditions, reversible electrocatalytic activity for H⁺/H₂ interconversion was observed (**Figure 14**) (94). Hydrogen is evolved at potentials just slightly negative compared to the thermodynamic equilibrium (no overpotential required) and anodic current density corresponding to hydrogen oxidation is measured for potentials positive to the thermodynamic equilibrium under H₂ supply.

Performance was assessed for GDL/MWCNT/[Ni(P₂^{CyN}₂^{Ester})]²⁺ (MWCNT = multi-walled carbon nanotube) in a half-cell floating electrode set-

up at ca. 15 mA cm⁻² (7.5 A mg_{Ni}⁻¹) at room temperature and 0.3 V vs. RHE, and ca. 40 mA cm⁻² (>20 A mg_{Ni}⁻¹) at 85°C, a technologically relevant operating temperature, and 0.3 V vs. RHE (53). This catalytic performance approaches that of a Pt nanoparticle-based electrode (Tanaka, 0.05 mg_{Pt} cm⁻²) benchmark under identical conditions. Proton reduction catalysis at room temperature reaches at 100 mV overpotential a current density of 7 mA cm⁻² at 25°C, and 38 mA cm⁻² at 85°C (**Figure 14**) (53). Some of these electrode materials furthermore proved quite stable with unchanged catalytic response over 10 hours of continuous operation. The H₂ oxidation current measured on GDL/MWCNT/[Ni(P₂^RN₂^{pyrene})₂] electrodes was found stable in the presence of 50 ppm CO, a feature likely shared by covalently immobilised NiP₂ species (93). Resistance to CO poisoning is thus another advantage of this series of catalysts over Pt nanoparticles, the surface of

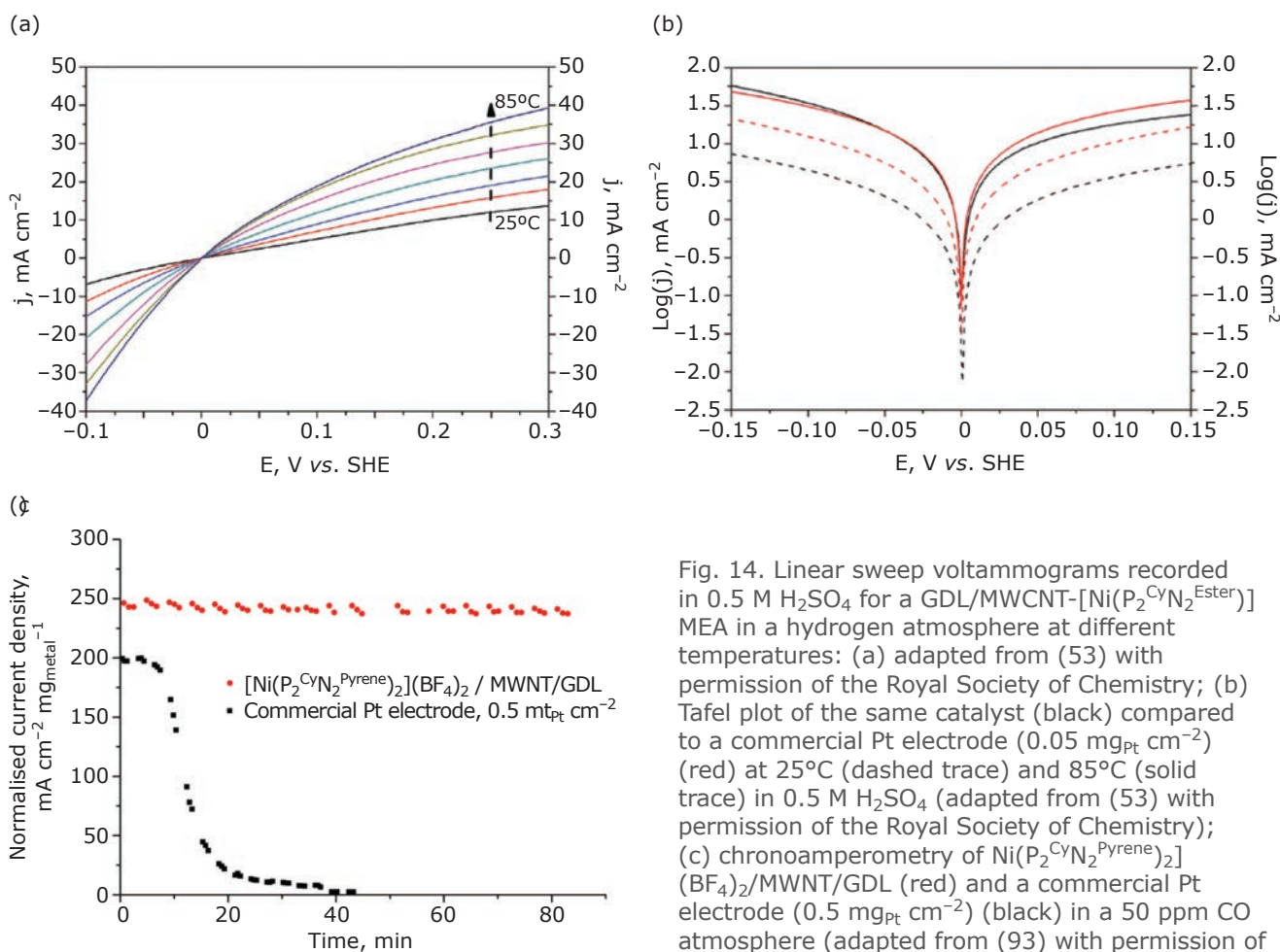


Fig. 14. Linear sweep voltammograms recorded in 0.5 M H₂SO₄ for a GDL/MWCNT-[Ni(P₂^{CyN}₂^{Ester})] MEA in a hydrogen atmosphere at different temperatures: (a) adapted from (53) with permission of the Royal Society of Chemistry; (b) Tafel plot of the same catalyst (black) compared to a commercial Pt electrode (0.05 mg_{Pt} cm⁻²) (red) at 25°C (dashed trace) and 85°C (solid trace) in 0.5 M H₂SO₄ (adapted from (53) with permission of the Royal Society of Chemistry); (c) chronoamperometry of Ni(P₂^{CyN}₂^{Pyrene})₂(BF₄)₂/MWNT/GDL (red) and a commercial Pt electrode (0.5 mg_{Pt} cm⁻²) (black) in a 50 ppm CO atmosphere (adapted from (93) with permission of Wiley)

which is irreversibly poisoned within a few minutes under sub-optimal conditions (**Figure 14(c)**).

In order to gain structural insights regarding the active species, X-ray absorption spectroscopy (XAS) at the Ni edge on GDL/MWCNT-[Ni(P₂^RN₂^{pyrene})₂] electrodes were measured (93). The XAS of immobilised [Ni(P₂^RN₂^{pyrene})₂]²⁺ species are quite similar, although not identical, to that of standalone [Ni(P₂^RN₂^{R'})₂]²⁺ complexes. As-prepared GDL/MWCNT-[Ni(P₂^RN₂^{pyrene})₂] electrodes also contain Ni(II) ions coordinated to light atoms attributed to solvent or water molecules, but these species are washed off during electrochemical equilibration in aqueous electrolytes (93). Of note, the XAS recorded at the Ni edge are found unchanged after 1 h of H₂ evolution or H₂ oxidation catalysis in aqueous H₂SO₄ 0.5 M solution, attesting for the stability of the grafted species (93).

These materials were implemented and shown to be operational in compact PEMFC prototypes (95, 93). An early fully operational Pt-free PEMFC was developed with MWCNT-[Ni(P₂^{Ph}N₂^{pyrene})₂]²⁺ at the anode, and a Co-N-C ORR catalyst (98, 99) at the cathode (93). An output power of 23 μW cm⁻² was obtained (**Figure 15**). More recently, the maximum power of a fuel cell integrating a SWNT-[Ni(P₂^{Cy}N₂^{Arg})₂]⁷⁺ (SWNT = single-walled nanotube) anode catalyst was measured just below 2 mW cm² (95). In that case, the limiting component is however a biocathode based on bilirubin oxidase immobilised on CNTs. Replacing this biocathode by a Pt-based cathode yielded a SWNT-[Ni(P₂^{Cy}N₂^{Arg})₂]⁷⁺-Pt/C PEMFC with a power

output of 14 mW cm⁻² at 0.47 V and 60°C, only seven times lower than a full-Pt PEMFC similarly built and operated under the same conditions (95).

4. Conclusions

Major breakthroughs have been achieved over the last decade in the design of catalysts based on Earth-abundant metals for catalysing the ORR or HOR, that are compatible with PEMFC technology and operate with overpotential requirements similar to those of conventional Pt catalysts. These catalysts are also more selective and therefore less sensitive to poisoning, a major asset for worldwide introduction of PEMFC technology if such innovative catalysts can be implemented in full devices while retaining other key specifications, i.e. power performance and durability. Still, progress has to be made in two directions. First, the electrochemical activities of such catalysts are still lower than those of optimised Pt-based catalysts. Closing the gap can be pursued by increasing the site density or the turnover frequency of the active sites, both for ORR and HOR noble metal-free catalysts. Additionally, specific optimisation of the catalyst layer structures for such catalysts could help promoting the power density reached for pgm-free H₂/air PEMFCs through a better control of protons and substrate/product diffusion together with avoidance of flooding. The other direction, in which it is urgent to invest, is the stability of the catalyst materials during representative drive cycles.

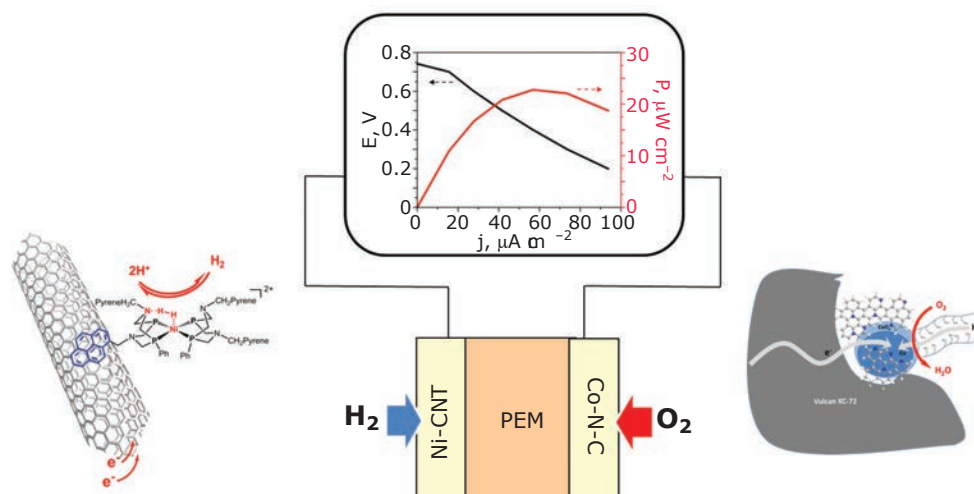


Fig. 15. Schematic representation of the PEMFC assembly from (93); the inset shows polarisation and power density curves recorded at 60°C with supply of partially humidified H₂ (20 ml min⁻¹) at the anode and passive air convection at the cathode. Adapted from (93) with permission of Wiley

Acknowledgements

This work was supported by the FCH Joint Undertaking (CRESCENDO Projet, Grant Agreement n°779366) and the Frenb National Research Agenç (Labex programme, ARCANE, ANR-11-LABX-0003-01). Goran Drazic from the National Institute of Chemistry, Ljubljana, Slovenia, is acknowledged for his work on the HR-STEM microscopy on the Fe-N-C catalyst from Centre National de la Recherche Scientifique (CNRS).

References

1. F. T. Wagner, B. Lakshmanan and M. F. Mathias, *J. Phys. Chem. Lett.*, 2010, **1**, (14), 2204
2. C. E. Thomas, *Int. J. Hydrogen Energy*, 2009, **34**, (15), 6005
3. J. Garback, T. Ramsden, K. Wipke, S. Sprik and J. Kurtz, 'Controlled Hydrogen Fleet and Infrastructure Demonstration and Validation Project', Workshop: Compressed Natural Gas and Hydrogen Fuels: Lessons Learned for the Safe Deployment of Vehicles, National Renewable Energy Laboratory of the US Department of Transportation and US Department of Energy, Washington, DC, USA, 10th–11th December, 2009
4. "Global Transport Scenarios 2050", World Energy Council, London, UK, 2011, 76 pp
5. O. Gröger, H. A. Gasteiger and J.-P. Suchsland, *J. Electrochem. Soc.*, 2015, **162**, (14), A2605
6. H. R. Ellamla, I. Staffell, P. Bujlo, B. G. Pollet and S. Pasupathi, *J. Power Sources*, 2015, **293**, 312
7. B. D. James, J. M. Huya-Kouadio, C. Houchins and D. A. DeSantis, "Mass Production Cost Estimation of Direct H₂ PEM Fuel Cell Systems for Transportation Applications: 2016 Update", Rev. 3, Strategic Analysis Inc, Arlington, USA, January, 2017, 244 pp
8. "Fuel Cell Technologies Office: Multi-Year Research, Development, and Demonstration Plan: Planned Program Activities for 2011-2020", Office of Energy Efficiency and Renewable Energy, Washington, DC, USA, 2013
9. G. Wu and P. Zelenay, *Acc. Chem. Res.*, 2013, **46**, (8), 1878
10. F. Jaouen, 'Heat-Treated Transition Metal-N_xC_y Electrocatalysts for the O₂ Reduction in Acid PEM Fuel Cells', in "Non-Noble Metal Fuel Cell Catalysts", eds. Z. Chen, J.-P. Dodelet and J. Zhang, Wiley-VCH Verlag GmbH & Co KGaA, Weinheim, Germany, 2014, pp. 29–118
11. A. Serov and C. Kwak, *Appl. Catal. B: Environ.*, 2009, **90**, (3–4), 313
12. A. Brouzgou, S. Q. Song and P. Tsiakaras, *Appl. Catal. B: Environ.*, 2012, **127**, 371
13. H. A. Gasteiger, J. E. Panels and S. G. Yan, *J. Power Sources*, 2004, **127**, (1–2), 162
14. C. Chen, Y. Kang, Z. Huo, Z. Zhu, W. Huang, H. L. Xin, J. D. Snyder, D. Li, J. A. Herron, M. Mavrikakis, M. Chi, K. L. More, Y. Li, N. M. Markovic, G. A. Somorjai, P. Yang and V. R. Stamenkovic, *Science*, 2014, **343**, (6177), 1339
15. M. Li, Z. Zhao, T. Cheng, A. Fortunelli, C.-Y. Chen, R. Yu, Q. Zhang, L. Gu, B. V. Merinov, Z. Lin, E. Zhu, T. Yu, Q. Jia, J. Guo, L. Zhang, W. A. Goddard III, Y. Huang and X. Duan, *Science*, 2016, **354**, (6318), 1414
16. D. Banham and S. Ye, *ACS Energy Lett.*, 2017, **2**, (3), 629
17. A. Kongkanand and M. F. Mathias, *J. Phys. Chem. Lett.*, 2016, **7**, (7), 1127
18. N. Nonoyama, S. Okazaki, A. Z. Weber, Y. Ikogi and T. Yoshida, *J. Electrochem. Soc.*, 2011, **158**, (4), B416
19. Z. Chen, D. Higgins, A. Yu, L. Zhang and J. Zhang, *Energy Environ. Sci.*, 2011, **4**, (9), 3167
20. F. Jaouen, E. Proietti, M. Lefèvre, R. Chenitz, J.-P. Dodelet, G. Wu, H. T. Chung, C. M. Johnston and P. Zelenay, *Energy Environ. Sci.*, 2011, **4**, (1), 114
21. H. Fei, J. Dong, M. J. Arellano-Jiménez, G. Ye, N. D. Kim, E. L. G. Samuel, Z. Peng, Z. Zhu, F. Qin, J. Bao, M. J. Yacaman, P. M. Ajayan, D. Chen and J. M. Tour, *Nature Commun.*, 2015, **6**, 8668
22. H. T. Chung, D. A. Cullen, D. Higgins, B. T. Sneed, E. F. Holby, K. L. More and P. Zelenay, *Science*, 2017, **357**, (6350), 479
23. A. Zitolo, V. Goellner, V. Armel, M.-T. Sougrati, T. Mineva, L. Stievano, E. Fonda and F. Jaouen, *Nature Mater.*, 2015, **14**, (9), 937
24. N. Ramaswamy, U. Tylus, Q. Jia and S. Mukerjee, *J. Am. Chem. Soc.*, 2013, **135**, (41), 15443
25. A. Zitolo, N. Ranjbar-Sahraie, T. Mineva, J. Li, Q. Jia, S. Stamatina, G. F. Harrington, S. M. Lyth, P. Krtil, S. Mukerjee, E. Fonda and F. Jaouen, *Nature Commun.*, 2017, **8**, 957
26. "2017 Annual Work Plan and Budget", Fuel Cells and Hydrogen 2 Joint Undertaking (FCH2JU), Brussels, Belgium, 2017
27. 'Fuel Cell Technologies Office Annual FOA', Funding Number DE-FOA-0001647, Fuel Cells Technology Office, Office of Energy Efficiency and Renewable Energy (EERE), Washington, DC, USA, 18th November, 2016
28. 'Communication from the Commission to the European Parliament, the Council, the European Economic and Social Committee and the Committee of the Regions on the Review of the List of Critical Raw Materials for the EU and the Implementation of the Raw Materials Initiative', COM/2014/0297 final, 26th May, 2014

29. Ballard Power Systems Inc, 'Ballard to Offer World's First PEM Fuel Cell Product Using Non Precious Metal Catalyst', PR Newswire, New York, USA, 12th September, 2017
30. M. Lefèvre, E. Proietti, F. Jaouen and J.-P. Dodelet, *Science*, 2009, **324**, (5923), 71
31. E. Proietti, F. Jaouen, M. Lefèvre, N. Larouche, J. Tian, J. Herranz and J.-P. Dodelet, *Nature Commun.*, 2011, **2**, 416
32. E. F. Holby, G. Wu, P. Zelenay and C. D. Taylor, *J. Phys. Chem. C*, 2014, **118**, (26), 14388
33. W. Liang, J. Chen, Y. Liu and S. Chen, *ACS Catal.*, 2014, **4**, (11), 4170
34. J. Shui, C. Chen, L. Grabstanowicz, D. Zhao and D.-J. Liu, *Proc. Natl. Acad. Sci. USA*, 2015, **112**, (34), 10629
35. Y. Nabaee, S. Nagata, T. Hayakawa, H. Niwa, Y. Harada, M. Oshima, A. Isoda, A. Matsunaga, K. Tanaka and T. Aoki, *Sci. Rep.*, 2016, **6**, 23276
36. F. Jaouen, V. Goellner, M. Lefèvre, J. Herranz, E. Proietti and J. P. Dodelet, *Electrochim. Acta*, 2013, **87**, 619
37. J. Y. Cheon, T. Kim, Y. Choi, H. Y. Jeong, M. G. Kim, Y. J. Sa, J. Kim, Z. Lee, T.-H. Yang, K. Kwon, O. Terasaki, G.-G. Park, R. R. Adzic and S. H. Joo, *Sci. Rep.*, 2013, **3**, 2715
38. A. Serov, K. Artyushkova, E. Niangar, C. Wang, N. Dale, F. Jaouen, M.-T. Sougrati, Q. Jia, S. Mukerjee and P. Atanassov, *Nano Energy*, 2015, **16**, 293
39. V. Armel, S. Hindocha, F. Salles, S. Bennett, D. Jones and F. Jaouen, *J. Am. Chem. Soc.*, 2017, **139**, (1), 453
40. H. A. Gasteiger, S. S. Kocha, B. Sompalli and F. T. Wagner, *Appl. Catal. B: Environ.*, 2005, **56**, (1-2), 9
41. A. Morozan and F. Jaouen, *Energy Environ. Sci.*, 2012, **5**, (11), 9269
42. D. Zhao, J.-L. Shui, L. R. Grabstanowicz, C. Chen, S. M. Commet, T. Xu, J. Lu and D.-J. Liu, *Adv. Mater.*, 2014, **26**, (7), 1093
43. P. Su, H. Xiao, J. Zhao, Y. Yao, Z. Shao, C. Li and Q. Yang, *Chem. Sci.*, 2013, **4**, (7), 2941
44. F. Jaouen, M. Lefèvre, J.-P. Dodelet and M. Cai, *J. Phys. Chem. B*, 2006, **110**, (11), 5553
45. J. Anibal, H. G. Romero, N. D. Leonard, C. Gumeci, B. Halevi and S. C. Barton, *Appl. Catal. B: Environ.*, 2016, **198**, 32
46. I. Herrmann, U. I. Kramm, S. Fiechter and P. Bogdanoff, *Electrochim. Acta*, 2009, **54**, (18), 4275
47. S. Stariha, K. Artyushkova, A. Serov and P. Atanassov, *Int. J. Hydrogen Energy*, 2015, **40**, (42), 14676
48. G. Wu, K. L. More, C. M. Johnston and P. Zelenay, *Science*, 2011, **332**, (6028), 443
49. G. Wu, K. Artyushkova, M. Ferrandon, A. J. Kropf, D. Myers and P. Zelenay, *ECS Trans.*, 2009, **25**, (1), 1299
50. D. Malko, T. Lopes, E. Symianakis and A. R. Kucernak, *J. Mater. Chem. A*, 2016, **4**, (1), 142
51. T. R. Ralph and M. P. Hogarth, *Platinum Metals Rev.*, 2002, **46**, (3), 117
52. J. A. Varnell, E. C. M. Tse, C. E. Schulz, T. T. Fister, R. T. Haasch, J. Timoshenko, A. I. Frenkel and A. A. Gewirth, *Nature Commun.*, 2016, **7**, 12582
53. T. N. Huan, R. T. Jane, A. Benayad, L. Guetaz, P. D. Tran and V. Artero, *Energy Environ. Sci.*, 2016, **9**, (3), 940
54. F. Calle-Vallejo, J. Tymoczko, V. Colic, Q. H. Vu, M. D. Pohl, K. Morgenstern, D. Loffreda, P. Sautet, W. Schuhmann and A. S. Bandarenka, *Science*, 2015, **350**, (6257), 185
55. F. Calle-Vallejo, M. D. Pohl, D. Reinisch, D. Loffreda, P. Sautet and A. S. Bandarenka, *Chem. Sci.*, 2017, **8**, (3), 2283
56. S. Brüller, H.-W. Liang, U. I. Kramm, J. W. Krumpfer, X. Feng and K. Müllen, *J. Mater. Chem. A*, 2015, **3**, (47), 23799
57. A. Serov, M. H. Robson, M. Smolnik and P. Atanassov, *Electrochim. Acta*, 2012, **80**, 213
58. J. Y. Cheon, J. H. Kim, J. H. Kim, K. C. Goddeti, J. Y. Park and S. H. Joo, *J. Am. Chem. Soc.*, 2014, **136**, (25), 8875
59. U. I. Kramm, I. Abs-Wurmbach, I. Herrmann-Geppert, J. Radnik, S. Fiechter and P. Bogdanoff, *J. Electrochem. Soc.*, 2011, **158**, (1), B69
60. M. J. Workman, A. Serov, L. Tsui, P. Atanassov and K. Artyushkova, *ACS Energy Lett.*, 2017, **2**, (7), 1489
61. F. Charreteur, F. Jaouen, S. Ruggeri and J.-P. Dodelet, *Electrochim. Acta*, 2008, **53**, (6), 2925
62. F. Jaouen, J. Herranz, M. Lefèvre, J.-P. Dodelet, U. I. Kramm, I. Herrmann, P. Bogdanoff, J. Maruyama, T. Nagaoka, A. Garsuch, J. R. Dahn, T. Olson, S. Pylypenko, P. Atanassov and E. A. Ustinov, *ACS Appl. Mater. Interfaces.*, 2009, **1**, (8), 1623
63. C. Gumeci, N. Leonard, Y. Liu, S. McKinney, B. Halevi and S. C. Barton, *J. Mater. Chem. A*, 2015, **3**, (43), 21494
64. U. I. Kramm, I. Herrmann, S. Fiechter, G. Zehl, I. Zizak, I. Abs-Wurmbach, J. Radnik, I. Dorbandt and P. Bogdanoff, *ECS Trans.*, 2009, **25**, (1), 659
65. V. Goellner, V. Armel, A. Zitolo, E. Fonda and F. Jaouen, *J. Electrochem. Soc.*, 2015, **162**, (6), H403
66. F. Jaouen and J.-P. Dodelet, *Electrochim. Acta*, 2007, **52**, (19), 5975
67. U. I. Kramm, J. Herranz, N. Larouche, T. M. Arruda, M. Lefèvre, F. Jaouen, P. Bogdanoff, S. Fiechter, I. Abs-Wurmbach, S. Mukerjee and J.-P. Dodelet, *Phys. Chem. Chem. Phys.*, 2012, **14**, (33), 11673

68. M. S. Thorum, J. M. Hankett and A. A. Gewirth, *J. Phys. Chem. Lett.*, 2011, **2**, (4), 295
69. Q. Zhang, K. Mamtani, D. Jain, U. Ozkan and A. Asthagiri, *J. Phys. Chem. C*, 2016, **120**, (28), 15173
70. S. Gupta, C. Fierro and E. Yeager, *J. Electroanal. Chem. Interfacial Electrochem.*, 1991, **306**, (1-2), 239
71. W. Li, A. Yu, D. C. Higgins, B. G. Llanos and Z. Chen, *J. Am. Chem. Soc.*, 2010, **132**, (48), 17056
72. N. R. Sahraie, U. I. Kramm, J. Steinberg, Y. Zhang, A. Thomas, T. Reier, J.-P. Paraknowitsch and P. Strasser, *Nature Commun.*, 2015, **6**, 8618
73. D. Malko, A. Kucernak and T. Lopes, *Nature Commun.*, 2016, **7**, 13285
74. J. L. Kneebone, S. L. Daifuku, J. A. Kehl, G. Wu, H. T. Chung, M. Y. Hu, E. E. Alp, K. L. More, P. Zelenay, E. F. Holby and M. L. Neidig, *J. Phys. Chem. C*, 2017, **121**, (30), 16283
75. C. M. Zalitis, J. Sharman, E. Wright and A. R. Kucernak, *Electrochim. Acta*, 2015, **176**, 763
76. W. Sheng, A. P. Bivens, M. Myint, Z. Zhuang, R. V. Forest, Q. Fang, J. G. Chen and Y. Yan, *Energy Environ. Sci.*, 2014, **7**, (5), 1719
77. V. Sh. Palanker, R. A. Gajyev and D. V. Sokolsky, *Electrochim. Acta*, 1977, **22**, (2), 133
78. M. Nagai, M. Yoshida and H. Tominaga, *Electrochim. Acta*, 2007, **52**, (17), 5430
79. S. Izhar, M. Yoshida and M. Nagai, *Electrochim. Acta*, 2009, **54**, (4), 1255
80. D. R. McIntyre, G. T. Burstein and A. Vossen, *J. Power Sources*, 2002, **107**, (1), 67
81. S. Izhar and M. Nagai, *J. Power Sources*, 2008, **182**, (1), 52
82. K. Pandey, S. T. A. Islam, T. Happe and F. A. Armstrong, *Proc. Natl. Acad. Sci. USA*, 2017, **114**, (15), 3843
83. G. Berggren, A. Adamska, C. Lambertz, T. R. Simmons, J. Esselborn, M. Atta, S. Gambarelli, J.-M. Mousesca, E. Reijerse, W. Lubitz, T. Happe, V. Artero and M. Fontecave, *Nature*, 2013, **499**, (7456), 66
84. R. Hidalgo, P. A. Ash, A. J. Healy and K. A. Vincent, *Angew. Chem. Int. Ed.*, 2015, **54**, (24), 7110
85. A. D. Wilson, R. H. Newell, M. J. McNevin, J. T. Muckerman, M. R. DuBois and D. L. DuBois, *J. Am. Chem. Soc.*, 2006, **128**, (1), 358
86. C. J. Curtis, A. Miedaner, R. Ciancanelli, W. W. Ellis, B. C. Noll, M. R. DuBois and D. L. DuBois, *Inorg. Chem.*, 2003, **42**, (1), 216
87. D. L. DuBois, *Inorg. Chem.*, 2014, **53**, (8), 3935
88. B. Ginovska-Pangovska, A. Dutta, M. L. Reback, J. C. Linehan and W. J. Shaw, *Acc. Chem. Res.*, 2014, **47**, (8), 2621
89. S. E. Smith, J. Y. Yang, D. L. DuBois and R. M. Bullock, *Angew. Chem. Int. Ed.*, 2012, **51**, (13), 3152
90. A. Dutta, S. Lense, J. Hou, M. H. Engelhard, J. A. S. Roberts and W. J. Shaw, *J. Am. Chem. Soc.*, 2013, **135**, (49), 18490
91. A. Dutta, D. L. DuBois, J. A. S. Roberts and W. J. Shaw, *Proc. Natl. Acad. Sci. USA*, 2014, **111**, (46), 16286
92. A. Dutta, J. A. S. Roberts and W. J. Shaw, *Angew. Chem. Int. Ed.*, 2014, **53**, (25), 6487
93. P. D. Tran, A. Le Goff, J. Heidkamp, B. Jusselme, N. Guillet, S. Palacin, H. Dau, M. Fontecave and V. Artero, *Angew. Chem. Int. Ed.*, 2011, **50**, (6), 1371
94. A. Le Goff, V. Artero, B. Jusselme, P. D. Tran, N. Guillet, R. Métayé, A. Fihri, S. Palacin and M. Fontecave, *Science*, 2009, **326**, (5859), 1384
95. S. Gentil, N. Lalaoui, A. Dutta, Y. Nedellec, S. Cosnier, W. J. Shaw, V. Artero and A. Le Goff, *Angew. Chem. Int. Ed.*, 2017, **56**, (7), 1845
96. N. Coutard, N. Kaeffer and V. Artero, *Chem. Commun.*, 2016, **52**, (95), 13728
97. R. T. Jane, P. D. Tran, E. S. Andreiadis, J. Pécaut and V. Artero, *Comptes Rendus Chimie*, 2015, **18**, (7), 752
98. A. Morozan, P. Jégou, B. Jusselme and S. Palacin, *Phys. Chem. Chem. Phys.*, 2011, **13**, (48), 21600
99. A. Morozan, P. Jégou, M. Pinault, S. Campidelli, B. Jusselme and S. Palacin, *ChemSusChem*, 2012, **5**, (4), 647

The Authors



Frédéric Jaouen obtained his PhD at the Royal Institute of Technology (KTH), Stockholm, Sweden, in 2003 under the supervision of Professor Göran Lindbergh. From 2004 to 2011, he was a research associate in Professor Jean-Pol Dodelet's group at Institut National de la Recherche Scientifique (INRS), Canada, where he focused on non-precious metal catalysts for oxygen electro-reduction. In 2011, Frédéric Jaouen was awarded an excellence chair from the ANR and moved to Université de Montpellier, France, to pursue his research on novel pgm-free catalysts for electrochemical energy conversion devices as a CNRS research fellow. He currently coordinates the H2020 project CREATE on anion-exchange membrane fuel cells and electrolyzers and is strongly involved in several other European and national projects focusing on catalysts free of critical raw materials for O₂ and CO₂ reduction. He was awarded the academic research prize from the Energy division of the French Chemical Society in 2017.



Deborah J. Jones received her PhD in 1982 from the University of London, King's College, UK, under the supervision of John Emsley. After a period at Southampton University, UK, she moved to France first with a Royal Society Fellowship and then a European Commission Sectoral Grant in Non-Nuclear Energy at the University of Montpellier, France. She is currently Director of Research at CNRS, Associate Director of the Institute Charles Gerhardt for Molecular Chemistry and Materials in Montpellier and serves as vice-president of the International Society of Electrochemistry. Her interests encompass the development of membrane, catalyst and electrode materials for proton exchange membrane fuel cells and electrolyzers. She is a Fellow of the Electrochemical Society (2015) and recipient (2016) of the Sir William Grove award of the International Association for Hydrogen Energy.



Nathan Coutard graduated in 2015 from Université Pierre et Marie Curie in Paris, France. His master's internship in Professor Kylie Vincent's lab at University of Oxford, UK, aimed to study the regulatory hydrogenase from *Ralstonia eutropha* using *in operando* spectro-electrochemistry. His PhD project in Dr Vincent Artero's group aims to optimise and integrate bio-inspired catalysts in a functional proton-exchange membrane fuel cell. His work includes electrode nanostructuring, electrochemistry, catalyst design, synthesis and tinkering.



Vincent Artero studied at the Ecole Normale Supérieure, Ulm, Germany, and graduated with his PhD in Inorganic Chemistry at the Université Pierre et Marie Curie in Paris in 2000. After a post-doctoral stay in RWTH Aachen, Germany, in the group of Professor Ulrich Kölle, he moved to the CEA centre in Grenoble (Fundamental Research Division) in 2001 to develop bioinspired chemistry related to hydrogen production and artificial photosynthesis. He received the 'Grand Prix Mergier-Bourdeix de l'Académie des Sciences' (2011) and was granted a Starting Grant from the European Research Council (ERC 2012–17). He currently acts as Chair of the Scientific Advisory Board of the ARCANÉ Excellence Laboratory Network (LABEX) for bio-driven chemistry in Grenoble and as co-chair of the French Research Network (GDR) on solar fuels.



Peter Strasser is the chaired professor of Electrochemistry and Electrocatalysis in the Chemical Engineering Division of the Department of Chemistry at the Technical University Berlin, Germany. Prior to his appointment, he was Assistant Professor at the Department of Chemical and Biomolecular Engineering at the University of Houston, USA. Before moving to Houston, Professor Strasser served as Senior Member of staff at Symyx Technologies, Inc, USA. In 1999, he received his doctoral degree in Physical Chemistry and Electrochemistry from the Fritz-Haber-Institute of the Max-Planck-Society, Berlin, Germany, under the direction of Gerhard Ertl. Peter Strasser was awarded the Otto-Hahn Research Medal by the Max-Planck Society, the Otto Roelen medal for catalysis awarded by the German Catalysis Society and the Ertl Prize awarded by the Ertl Center for Catalysis.



Anthony Kucernak received his PhD from Southampton University, UK, in 1991 and carried out postdoctoral research at Cambridge University, UK. He subsequently moved to Imperial College London, UK, where he has held the post of Professor of Physical Chemistry since 2009. He has published more than seventy papers on novel methods for screening catalysts under realistic operating conditions; the study of individual catalyst particles and the modification of surface composition to probe the fundamentals of electrocatalysis. He has been an invited plenary speaker at the 2005 International Fuel Cell Workshop, Japan, and co-chaired the Gordon Conference on fuel cells in 2004. In 2006 he was awarded the Helmut Fisher medal for his work on fuel cell electrode structure and fundamental results in electrocatalysis.